JBC RESEARCH ARTICLE

Small molecule-based regulation of gene expression in human astrocytes switching on and off the G-quadruplex control systems

Received for publication, May 7, 2024, and in revised form, October 18, 2024 Published, Papers in Press, November 29, 2024,
https://doi.org/10.1016/j.jbc.2024.108040

Vijay Kumar M. J[1,‡], Jérémie Mitteaux[2,‡], Zi Wang[3], Ellery Wheeler[4], Nitin Tandon[4], Sung Yun Jung[5], Robert H. E. Hudson[3], David Monchaud[2,*], and Andrey S. Tsvetkov[1,6,7,*]

From the [1]The Department of Neurology, The University of Texas McGovern Medical School at Houston, Houston, Texas, USA; [2]Institut de Chimie Moléculaire de l'Université de Bourgogne (ICMUB), CNRS UMR6302, Dijon, France; [3]Department of Chemistry, The University of Western Ontario, London, Ontario, Canada; [4]The Department of Neurosurgery, The University of Texas, McGovern Medical School at Houston, Houston, Texas, USA; [5]Department of Biochemistry and Molecular Pharmacology, Baylor College of Medicine, Houston, Texas, USA; [6]The University of Texas Graduate School of Biomedical Sciences, Houston, Texas, USA; [7]UTHealth Consortium on Aging, The University of Texas McGovern Medical School, Houston, Texas, USA

Reviewed by members of the JBC Editorial Board. Edited by Patrick Sung

A great deal of attention is being paid to strategies seeking to uncover the biology of the four-stranded nucleic acid structure G-quadruplex (G4) *via* their stabilization in cells with G4-specific ligands. The conventional definition of chemical biology implies that a complete assessment of G4 biology can only be achieved by implementing a complementary approach involving the destabilization of cellular G4s by *ad hoc* molecular effectors. We report here on an unprecedented comparison of the cellular consequences of G4 chemical stabilization by pyridostatin (PDS) and destabilization by phenylpyrrolocytosine (PhpC) at both transcriptome- and proteome-wide scales in patient-derived primary human astrocytes. Our results show that the stabilization of G4s by PDS triggers the dysregulation of many cellular circuitries, the most drastic effects originating in the downregulation of 354 transcripts and 158 proteins primarily involved in RNA transactions. In contrast, destabilization of G4s by PhpC modulates the G4 landscapes in a far more focused manner with upregulation of 295 proteins, mostly involved in RNA transactions as well, thus mirroring the effects of PDS. Our study is the first of its kind to report the extent of G4-associated cellular circuitries in human cells by systematically pitting the effect of G4 stabilization against destabilization in a direct and unbiased manner.

Chemical biology (1) hinges on the strategic use of small molecule modulators to disrupt cellular equilibria reversibly, both spatially and temporally (2). The responses of cells to these molecular effectors are then analyzed to gain insights into underlying molecular mechanisms. For accurate and dependable interpretations, interventions in chemical biology rely on exquisitely specific molecular tools to prevent off-target effects and potential misinterpretations of molecular mechanisms. Ideally, chemical biologists should use both positive and negative regulators to ensure a balanced assessment of the cellular circuitry being studied, thereby enhancing the reliability of their findings (3).

Recently, the field of DNA and RNA G-quadruplexes (G4s) (4–7) has become a favorite playground for chemical biologists (8) eager to uncover new levels of regulation of gene expression referred to as G4omics (9, 10). G4 is a four-stranded nucleic acid structure (Fig. 1*A*) that assembles from guanine (G)-rich DNA or RNA sequences when freed from their hybridized forms (*e.g.*, duplex for DNA, stem-loop for RNA) (11). The G4-forming sequences are widespread in our genome and transcriptome, >1 million putative G4 sequences are predicted by G4Hunter (DNA) (12) and G4RNA Screener (RNA) (13). G4s fold thanks to the formation and self-stacking of cyclic arrays of Gs known as G-quartets; despite very high thermodynamic stability, they undergo rapid folding and unfolding orchestrated by the G4 chaperones (14) and G4 helicases (15), respectively, which intervene in virtually all DNA- and RNA-dependent processes. This explains why mutations in G4 helicase-coding genes are linked to multiple life-threatening diseases, including inheritable genetic diseases (*e.g.*, WRN is mutated in Werner syndrome, RTEL1 in dyskeratosis congenita, XPD in xeroderma pigmentosum and Cockayne syndrome), cancers and aging phenotypes (15–19).

Chemical biologists aspire to substitute proteins with small molecules that offer greater practical convenience. They have developed numerous G4 molecular chaperones or G4 ligands (20) that have been used to (i) demonstrate the existence and prevalence of DNA and RNA G4s in human cells (21); (ii) provide insights into the regulation of gene expression at both transcriptional and translational levels (6, 22), and (iii) advance chemotherapeutic strategies that leverage G4s as genetic tools to impede the progression of diseases, especially cancers (23). In sharp contrast, the development of G4 molecular helicases or G4 destabilizers is still in its infancy (17, 24). While many G4 stabilizers have been used in yeast, cancer cells, and more

‡ Authors contributed equally to this work.
* For correspondence: Andrey S. Tsvetkov, andrey.s.tsvetkov@uth.tmc.edu; David Monchaud, david.monchaud@u-bourgogne.fr.

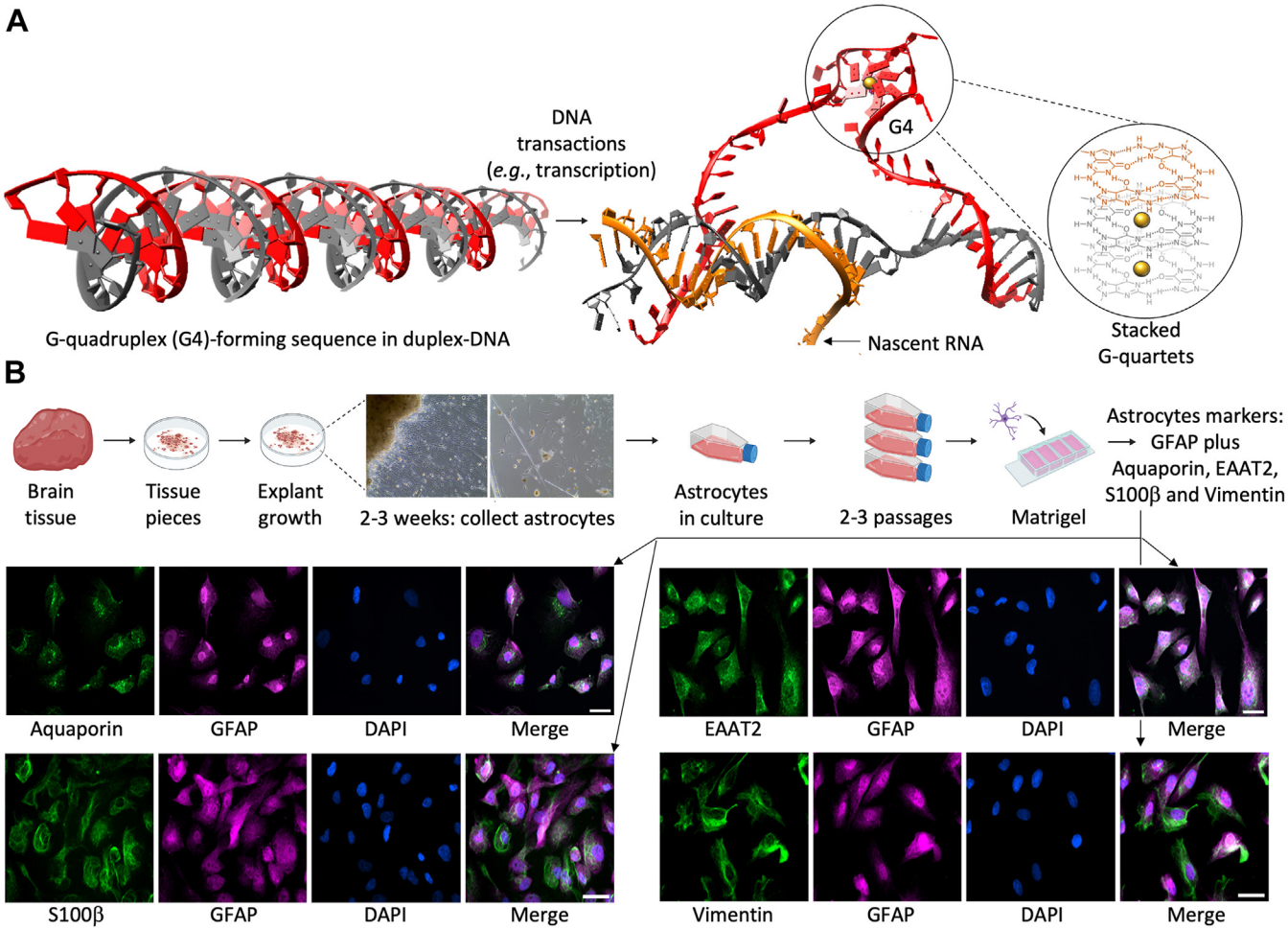

Figure 1. Schematic model for human astrocyte culture. *A*, representation of the formation of a G4 structure originating in the release of the G4-forming sequence from its duplex constraint (right panel: highlight on the self-stacking of G-quartets that form the core of the G4 structure). *B*, primary human astrocytes were cultured from the frontal lobes of brain explants cultured in DMEM medium supplemented with FBS and growth factors before being collected for immunostaining: the purity of astrocyte cultures was checked by staining using the specific astrocyte markers aquaporin, EAAT2, S100β or vimentin (*green*), GFAP (*magenta*), and nuclear dye DAPI (*blue*). Samples were imaged with a confocal microscope. Scale bar, 10 μm.

recently in brain cells (*vide infra*), only a few G4 destabilizers have been developed so far (25–30), and their studies were limited to *in vitro* investigations. Only a phenylpyrrolocytosine referred to as PhpC (29) has been identified as a reliable negative regulator of G4s in human cancer cells by both optical imaging and G4-RNA-specific affinity precipitation (G4RP) techniques (31, 32).

We aim here to assess the properties of PhpC in primary human astrocytes, major brain cells critically involved in age-associated brain disorders. Indeed, we recently provided evidence of the involvement of G4s in aging phenotypes, showing that (i) aged mouse brains contain higher levels of G4s than young brains (33), (ii) the stabilization of G4s with the small molecule stabilizer pyridostatin (PDS) (34) promotes genomic instability in neurons, astrocytes, and microglial cells (35–37), and *iii*-mice injected with PDS exhibit cognitive impairment and accelerated aging (33), reminiscent of what was described in *C. elegans* (38). Aging, indeed, provides a permissive chromatin environment for G4s: beyond multiple epigenetic and epitranscriptomic changes, condensed heterochromatic regions are diminished during aging (39–42), with a frequent loss of nucleosomes, which provides a window of opportunity for G4-forming sequences to fold. G4s might thus be important in aging cells, but at present, the associated molecular mechanisms are largely unknown.

The goal of the present study is to establish a firm connection between G4 stabilization and destabilization and nervous cell biology (19, 43, 44). To this end, our approach abides by the aforementioned definition of chemical biology, using both positive (PDS) and negative (PhpC) modulators of G4s in human astrocytes. We selected these molecules owing to their established selectivity for G4s over other nucleic acid structures (29, 31, 34, 45, 46). They are both pan-G4 ligands, *i.e.*, prone to interact with any type of DNA/RNA G4s: this was demonstrated for instance by the use of PDS for assessing the prevalence of G4s in the human genome (by G4-seq) (47) and transcriptome (by rG4-seq) (48), and the use of PhpC to unfold both DNA G4s (49–51) (notably by BG-flow) (49) and RNA G4s (31, 50) (notably by G4RP) (31) in human cells. This is a desirable feature here, as we aimed at using these molecular

tools to interact with any type of cellular G4s. We selected astrocytes because they *i*-have a significant role in neuronal function, physiology, and overall brain development (52), *ii*-are well-accepted cell candidates for uncovering the pathophysiology of neurological disorders (considering their myriad roles in brain homeostasis), and *iii*-are practically convenient due to their ability to replicate and divide (53–56). We used transcriptome-wide gene expression analysis (RNA-seq) and proteome-wide mass spectrometry (MS) analysis to identify the molecular pathways affected by PhpC or PDS. Our results show that G4s are indeed key genetic levers in astrocytes: PDS displays a strong inhibitory activity at both transcriptome- and proteome-wide scale, and PhpC affects the proteome of astrocytes only, positively contributing to the regulation of RNA processes, stress response, and cellular internal organization. Thus, G4s are interesting chemical biology targets in human astrocytes, and their destabilization by *ad hoc* molecular effectors might represent a relevant strategy to alleviate G4-associated dysfunctions.

Results

Astrocytes were cultured from explants derived from the frontal lobes of human brain resections obtained from a 32-year-old patient. The astrocytic phenotype of these isolated cells was rigorously confirmed by immunostaining with a panel of well-established astrocyte-specific markers, including glial fibrillary acidic protein (GFAP) (57) plus aquaporin (58), excitatory amino acid transporter 2 (EAAT2) (59), calcium-binding protein S100β (60) and vimentin (61) (Figure 1*B* and Supplementary Fig. S1).

We first performed RNA-seq analysis for human astrocytes treated with 2 μM PDS for 24 h (Fig. 2). The RNA-seq data featured high quality across all samples (Supplementary Fig. S2). The principal component analysis of this set of results highlighted clear distinctions between the untreated controls *versus* PDS-treated cells: we identified 516 (2.7%) differentially expressed genes (DEGs) out of a pool of 18,648 genes with measured expression. Among these 516 DEGs, 162 genes (31%) were upregulated, and 354 genes (69%) were downregulated (Fig. 2*A* and Supplementary Fig. S4). PDS treatment, thus, strongly alters the transcriptome of astrocytes, modulating the expression of an extended network of genes, in line with previous reports in different cell types (37, 62).

We then conducted data mining within the context of both pathways (Kyoto Encyclopedia of Genes and Genomes (KEGG) database) (63) and gene ontologies (Gene Ontology (GO) consortium database) (64, 65), implementing iPathwayGuide (Advaita Bioinformatics) (66), using the probability (p) value as a significance marker, considered to be high confidence when $p \leq 0.01$. Our analysis revealed significant modifications encompassing 5403 GO terms and 233 KEGG terms related to 28 pathways. The most enriched pathways were *i*-the regulation of cell cycle (31 out of 124 DEGs, 25%), including the cellular stress/DNA damage response protein GADD45 G, p = 2.0e-3), *ii*-homologous recombination (9 out of 41 DEGs, 22%, DNA repair family (see the supplementary data for definition), including the helicase BLM and the recombinase RAD51, p = 1.0e-6), *iii*- DNA replication (12 out of 36 DEGs, 33%, including the helicase DNA2 (p = 4.3e-5) and the structure-specific endonuclease FEN1, p = 1.0e-6) and *iv*-the Fanconi anemia pathway (12 out of 54 DEGs, 22%, disease family, including the helicase FANCJ and the repair proteins BRCA1 and BRCA2, p = 1.0e-6) (Fig. 2*C*). Among the most notable downregulated genes were helicases (20 out of 72 DEGs, 27%, including the G4 helicases BLM, FANCJ, and PIF1, p = 1.0e-6) and repair proteins (both double-strand break repair (39 out of 246 DEGs, 16%) and recombinational repair (30 out of 139 DEGs, 22%), including RAD51, BRCA1 and BRCA2, p = 1.0e-6, Fig. 2*C*). These results make PDS a double-edged sword as it concomitantly inhibits G4 helicases, which triggers an increase in G4s, that is, in G4-mediated DNA damage (46, 67), and DNA repair proteins (68), which hampers the proper repair of this damage.

In sharp contrast, PhpC-treated human astrocytes (20 μM for 24 h) experienced an almost insignificant transcriptomic change. We identified only nine DEGs (0.1%) out of 15,309 genes with measured expression. Among these nine DEGs, only one gene (11%) was downregulated, and eight genes (89%) were upregulated (Fig. 2*B*). The treatment of PhpC thus triggers the modification of only 581 GO terms and 12 KEGG terms (with moderate significance, $p < 0.6$), related to five pathways but in a minimal manner. Expression of only 1 to 4% of RNA (from one out of 22 DEGs (hormone biosynthesis) to two out of 129 DEGs (ligand-receptor interactions)) were modified (again with moderate significance, $p < 0.05$, Fig. 2*C*). Collectively, these results indicate that PhpC does not affect transcription, which could be interpreted as evidence that PhpC does not act on G4 DNA in human astrocytes. We nevertheless compared the gene expression common between PDS- and PhpC-treated astrocytes and identified only two common DEGs (ADRA2C and ANKHD1-EIF4EBP3, $p < 0.01$), but not related to any recognized cellular pathway.

To investigate further the properties of these two molecular effectors, we focused on proteomics (mass spectrometry, MS, Supplementary Fig. S3). Similar to the RNA-seq analysis, PDS-treated astrocytes experienced a series of significant changes, compared to the untreated control (Fig. 3 and Supplementary Figs. S5 and S6). We identified 381 (10.6%) differentially expressed proteins (DEPs) out of a pool of 3604 proteins with measured expression. Among these 381 DEPs, 223 proteins (58%) were upregulated, and 158 proteins (42%) were downregulated (Fig. 3*A*). Our study shows that PDS influences 256 KEGG terms and 4955 GO terms related to 12 pathways. The most significantly impacted pathways include chromatin assembly (31 out of 80 DEPs, 39%), nucleosome assembly (29 out of 73 DEPs, 40%), DNA packaging (31 out of 92 DEPs, 34%), all belonging to the chromatin modification and organization family, DNA conformation change (36 out of 127 DEPs, 28%), telomere organization (23 out of 80 DEPs, 29%), and ribonucleoprotein complex biogenesis (38 out of 237 DEPs, 16%) among others. These modifications include the dysregulation of the remodeler ATRX (p = 0.01, helicase family) and both the

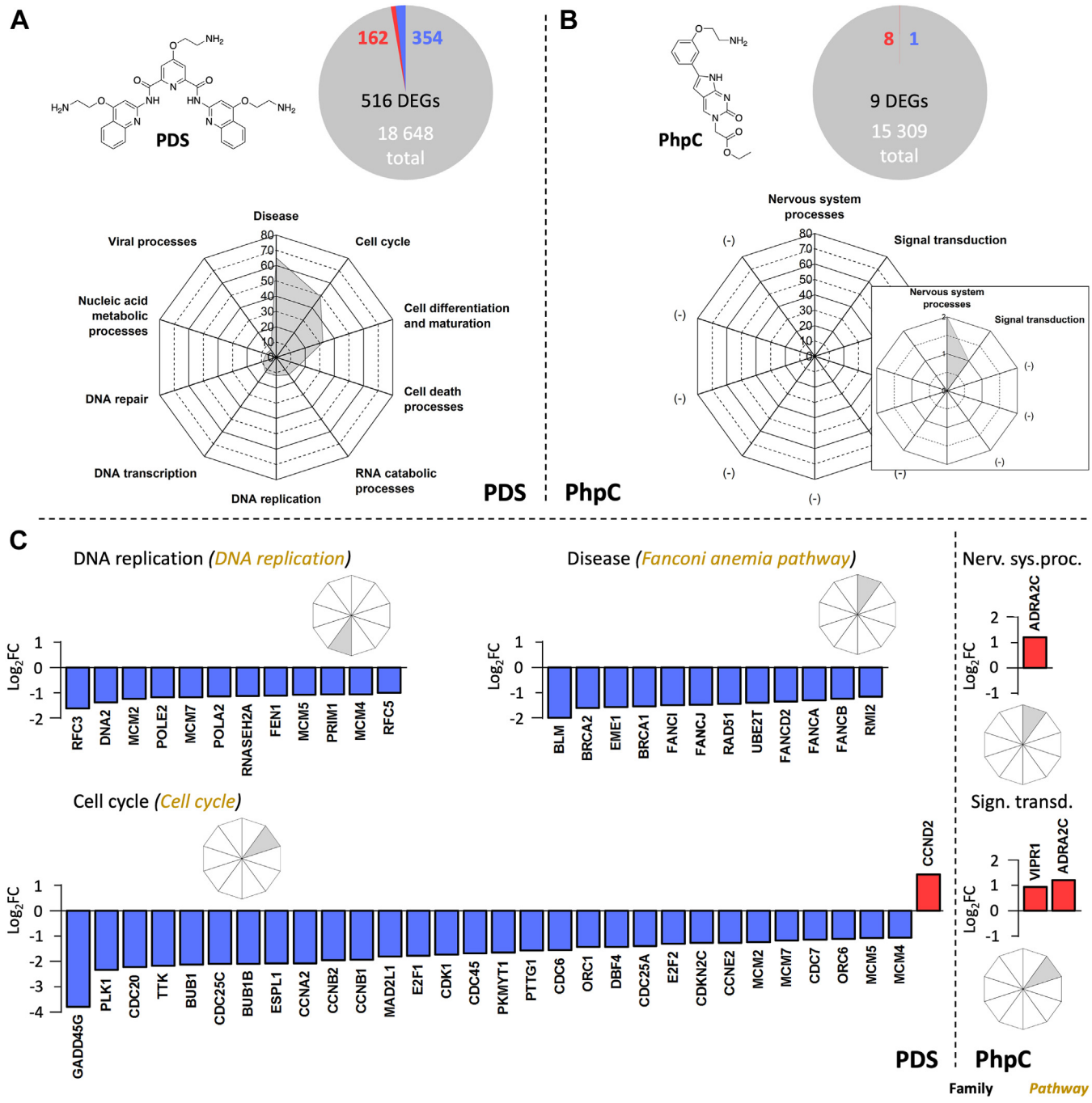

Figure 2. G4 stabilizer PDS and destabilizer PhpC alters transcription in human astrocytes. *A*, PDS alters the expression of 516 genes (DEGs) in human astrocytes represented in the pie chart and dysregulated biological pathways shown in the radar plot. *B*, human astrocytes upon being treated with PhpC dysregulated nine genes shown in pie chart and modified biological pathways are represented in radar plot. *A/B*, numbers in the pie charts: in *white*: genes with measured expression; in *black*: DEGs; in *red*: upregulated genes; in *blue*: downregulated genes. *C*, examples of downregulated (*blue*) or upregulated (*red*) transcripts related to DNA replication, Fanconi anemia, and cell cycle upon incubation with either PDS (*left panel*) or PhpC (*right panel*) in human astrocytes (see the supplementary data for definition). The threshold used to select the DE genes was 0.6 for expression change and 0.05 for significance. Log_2FC represents the ratio of normalized gene expression in PDS and PhpC treatment. 0 – no change, positive value – increase in expression, negative value – decrease in expression.

structure-specific endonuclease FEN1 (p = 0.02) and the DNA polymerase cofactor PCNA (p = 0.04), belonging to the cellular component organization or biogenesis family (Fig. 3*C*). Among the DEPs, the helicases were affected (13 out of 77 DEPs, 17%) but diversely. Eight were upregulated (DHX8, DDX10, ERCC3, DDX60 and DDX39B, p = 1.0e-6; DDX24, ATRX and DDX1, $p < 0.03$) and five were downregulated (DDX58 and ERCC6L, p = 1.0e-6; MCM6, EIF4A1 and DHX15, $p < 0.04$) (Fig. 3*C*). Similarly, DNA repair proteins were diversely dysregulated (both double-strand break repair (7 out of 52 DEPs, 13%) and recombinational repair (5 out of 30 DEPs, 17%), but not in a significant manner ($p \geq 0.5$). These results indicated that the

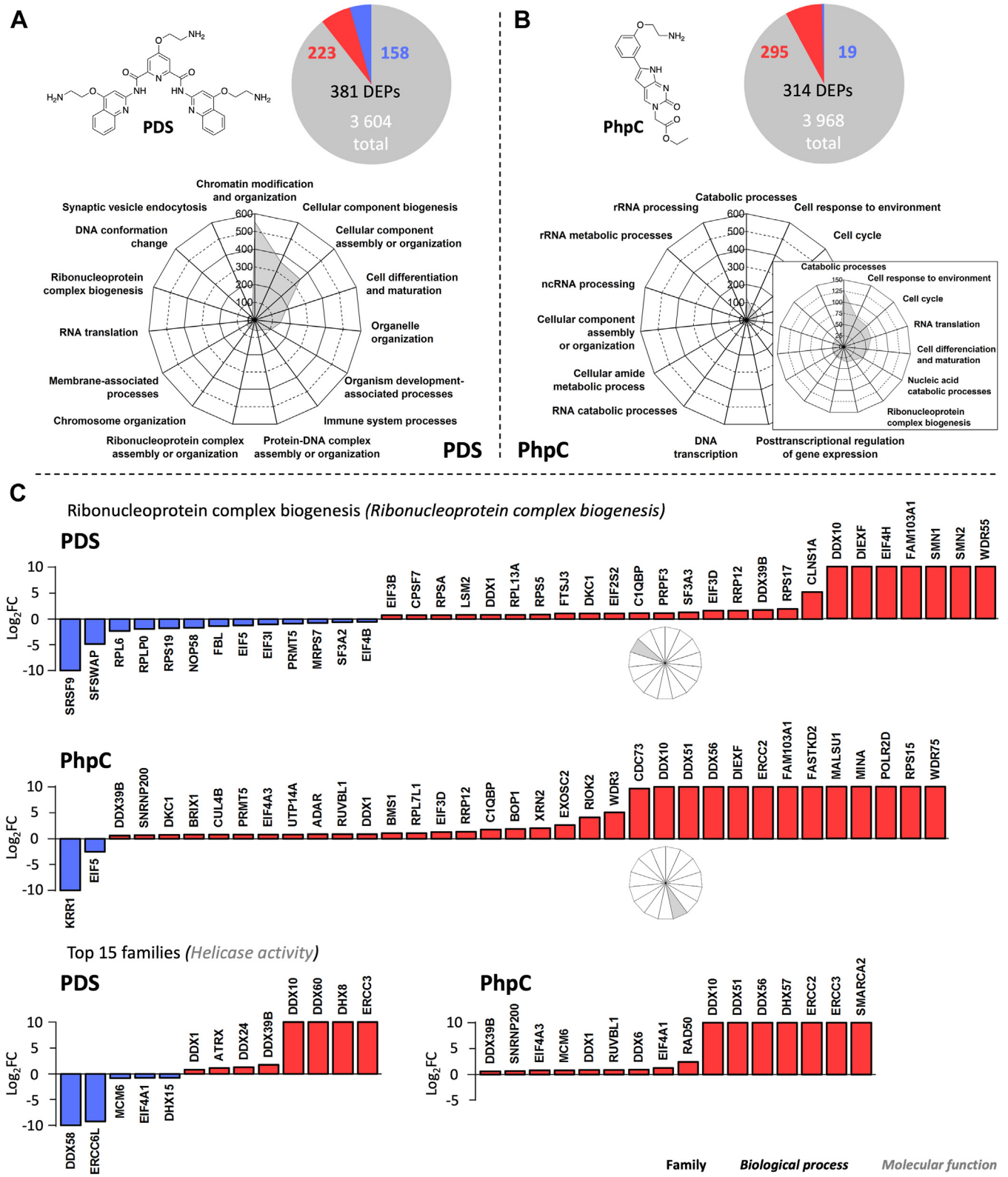

Figure 3. G4 stabilizer PDS and destabilizer PhpC alters translation in human astrocytes. *A*, PDS modifies the expression of 381 proteins (DEPs) of human astrocytes represented in pie chart and dysregulated biological pathways are shown in radar plot. *B*, PhpC alters the expression of 314 proteins (DEPs) in human astrocytes shown in pie chart and dysregulated biological pathways represented in the radar plot. *A/B*, numbers in the pie charts: in *white*: genes with measured expression; in *black*: DEGs; in *red*: upregulated genes; in *blue*: downregulated genes. *C*, examples of transcripts downregulated (*blue*) or upregulated (*red*) upon incubation with either PDS or PhpC belonging to ribonucleoprotein complex biogenesis and helicase activity (see the supplementary data). Log_2FC represents the ratio of normalized gene expression in PDS and PhpC treatment. 0 – no change, positive value – increase in expression, negative value – decrease in expression.

modulation of the proteome triggered by PDS is a comprehensive but complex and multi-level process.

Compared to RNA-seq results, proteomic changes triggered by PhpC were much more significant: we identified 314 DEPs (7.9%) out of 3968 proteins with measured expression. Among 314 DEPs, 295 proteins (94%) were upregulated, whereas only 19 proteins (6%) were downregulated (Fig. 3*B* and Supplementary Figs. S7 and S8). These results confirm that PhpC has more impact on translational *versus* transcriptional activity in astrocytes. These modifications include 260 KEGG terms and 4485 GO terms related to 16 pathways. Among them, the most notable pathways include base-excision repair (4 out of 16 DEPs, 25%, including FEN1, p = 1.0e-6). The cellular processes affected are P-body assembly (4 out of 10 DEPs, 40%, including DDX6, p = 0.05), DNA transcription (8 out of 38 DEPs, 21%, including DDX39B, p = 0.03), regulation of RNA stability (13 out of 77 DEPs, 17%, including FUS, p = 1.0e-6, RNA stability), DNA duplex unwinding (6 out of 40 DEPs, 15%, including DDX1, p = 0.03, DNA repair), and regulation of translation (26 out of 188 DEPs, 14%, including EIF5, p = 1.0e-6, RNA translation), among others (Fig. 3*C*). As mentioned earlier, among the DEPs, both helicases (with the upregulation of 16 out of 83 helicases (19%), eight being statistically relevant, DDX10, DDX51, DDX56, ERCC2, ERCC3, DHX57, SMARCA2, and MCM6, p = 1.0e-6) (Fig. 3*C*) and DNA damage binding proteins rank high (with the upregulation of six out of 24 proteins (25%), four being statistically relevant, FEN1, ERCC2, ERCC3, and RAD23B, p = 1.0e-6).

Next, we investigated the common proteins between PDS and PhpC datasets. The expression of 107 proteins was found to be dysregulated by the two compounds (Figure 4*A* and Supplementary Fig. S9), including 92 upregulated proteins (86%) in both instances (hereafter called $PDS^+/PhpC^+$), five downregulated (5%) in both cases ($PDS^-/PhpC^-$), and 10 differently expressed (9%), with nine $PDS^-/PhpC^+$ and only one $PDS^+/PhpC^-$ (NUCKS1, $p < 0.02$). We found 33 biological processes dysregulated by both PDS and PhpC, including the significantly affected regulation of protein binding (22–27% of dysregulated proteins out of >30 proteins, p = 5.0e-3, protein binding family), ribonucleoprotein complex biogenesis (14–16% of >200 proteins, p = 3.8e-4, ribonucleoprotein complex biogenesis family) and cellular component organization (8–12% of >1700 proteins, p = 7.0e-4, cellular component assembly or organization family) (Fig. 4*B*), which are all related to the translation machinery.

To gain more accurate insights into the cellular circuitries dysregulated by PDS, PhpC, or both, we performed a STRING analysis (69), which computationally estimates (databases aggregation) the probability of both direct (physical) and indirect (functional) interactions between two proteins *via* a strength (s) score, considered to be high confidence when $s \geq 0.70$. We found that the 223 PDS^+ proteins are involved in RNA transactions (Fig. 4*C*), including cytoplasmic translation (12 out of 123 proteins, 10%, s = 0.94) and regulation of mRNA processing (9 out of 140 proteins, 6%, s = 0.76), in ribonucleoprotein complex subunit assembly (16 out of 203 proteins, 8%, s = 0.84) and organization (17 out of 211 proteins, 8%, s = 0.85) and DNA binding (6 out of 58 proteins, 3%, s = 0.96). In contrast, the 158 PDS^- proteins (Fig. 4*D*) are primarily involved in cell organization (*e.g.*, RNA localization (8 out of 180 proteins, 4%, s = 0.79) and protein localization to the nucleus (8 out of 195 proteins, 4%, s = 0.75) or membrane (10 out of 219 proteins, 5%, s = 0.80)) and chromatin organization (*e.g.*, nucleosome organization (16 out of 162 proteins, 10%, s = 1.13) and assembly (15 out of 124 proteins, 12%, s = 1.22)).

Next, we focused on the 295 $PhpC^+$ proteins (Fig. 4*E*) and found that they are also involved in RNA transactions, including rRNA processing (19 out of 220 proteins, 9%, s = 0.76) and metabolic process (20 out of 250 proteins, 8%, s = 0.73), ribosome (24 out of 299 proteins, 8%, s = 0.73) and ribonucleoprotein complex biogenesis (34 out of 449 proteins, 8%, s = 0.71). Notably, proteins involved in P-body assembly (4 out of 14 proteins, 29%, s = 1.28) rank high, contributing to RNA transactions (degradation and silencing) (70). In sharp contrast, the 19 $PhpC^-$ proteins do not belong to any identifiable network, as do the five $PDS^-/PhpC^-$, nine $PDS^-/PhpC^+$, and one $PDS^+/PhpC^-$ proteins (Fig. 4*F*), likely due to their low number. The 92 $PDS^+/PhpC^+$ proteins (Fig. 4*F*) primarily intervene in protein dephosphorylation (4 out of 34 proteins, 12%, s = 1.4), epithelial cell morphogenesis (4 out of 34 proteins, 12%, s = 1.4) and more generally binding interactions (10 out of 375 proteins, 3%, s = 0.76), but also in cellular component biogenesis (11 out of 500 proteins, 2%), localization (29 out of 2677 proteins, 1%) and organization (both cellular (48 out of 5639 proteins, 0.9%) and organelle organization (37 out of 3470 proteins, 1%)), although in a non-significant manner ($s < 0.7$). Interestingly, the molecular components that are most affected by both PDS and PhpC are associated with stress granules (7 out of 84 proteins, 8%, s = 1.25) and polysome formation (5 out of 65 proteins, 8%, s = 1.22), fully in line with the pivotal role played by G4s in response to cellular stress and translation (71–73).

Notably, both PDS and PhpC strongly impact RNA metabolism, although through different angles. PDS triggers a scatter-gun type of damage, affecting most if not all cellular circuitries, which is in line with the RNA-seq analysis: indeed, the 354 PDS^- transcripts belong to dozens of different cellular pathways (including DNA repair (62 out of 497 DEGs, 13%), replication (51 out of 203 DEGs, 25%) and unwinding (25 out of 89 DEGs, 28%)), and quite surprisingly, the 162 PDS^+ transcript do not belong to any identifiable network. This suggests that the cellular effects of PDS originate in its ability to downregulate cellular processes, acting at both transcriptional and translational levels (*i.e.*, on both DNA and RNA G4s). In sharp contrast, PhpC has a narrower spectrum of action, acting solely at the translational level (*i.e.*, on RNA G4s) and solely as an activating agent, positively regulating RNA processes, stress responses, and cellular internal organization.

Altogether, these results indicate that even if PDS and PhpC share the same targets (G4s), their cellular responses are strongly different, which is fully in line with the type of interaction they intend to have with G4s (stabilization *versus* destabilization). However, G4 involvement in the cellular pathways and biological processes described above remained,

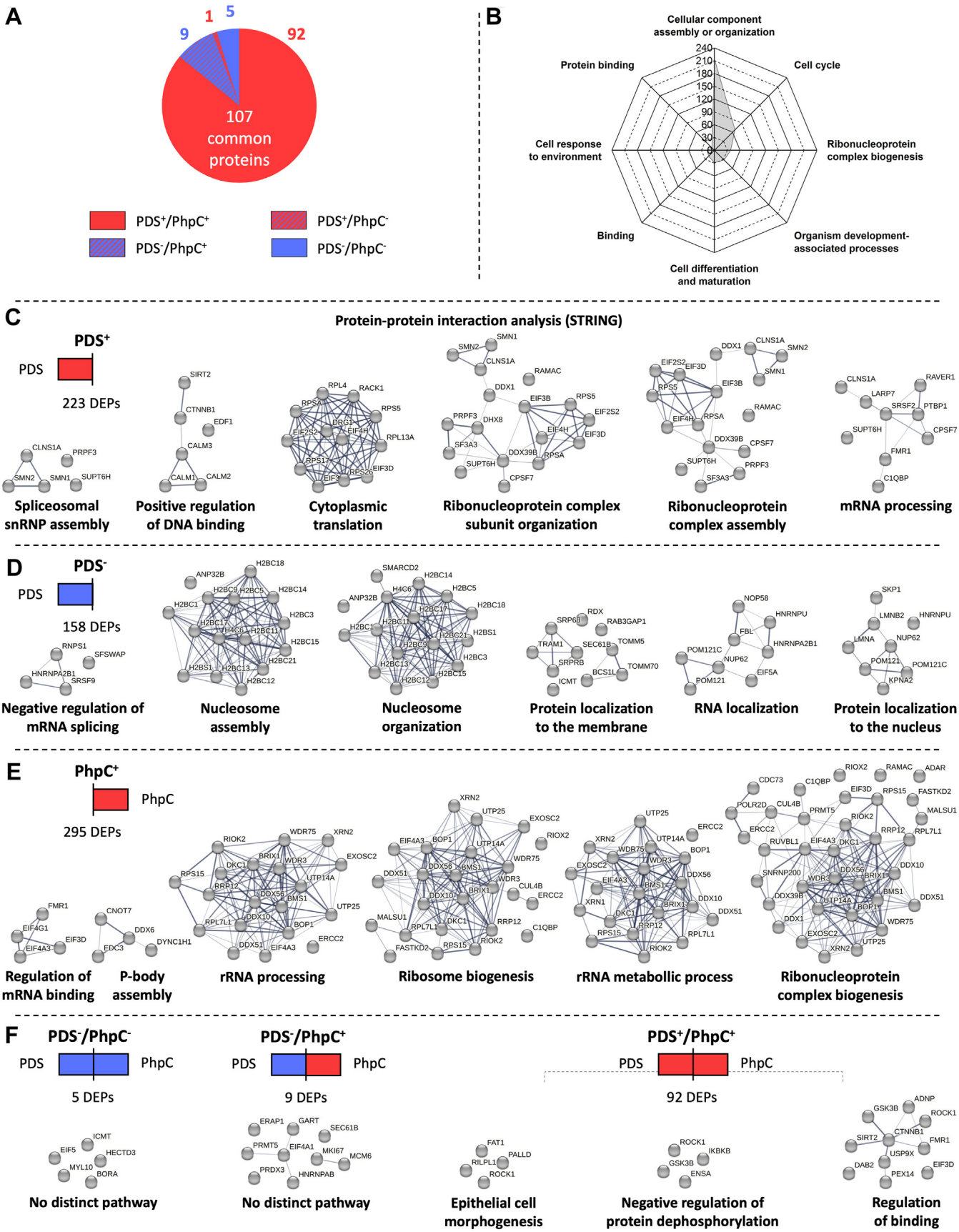

Figure 4. A meta-analysis comparing common proteins and pathways altered by PDS and PhpC. *A*, the pie chart represents the common DEPs shared either with PDS0- or PhpC-treated human astrocytes. *B*, the radar plot shows the common dysregulated biological pathways in human astrocytes treated with PDS or PhpC. *C*, the string protein-protein interaction analysis showing the examples of enrichment maps of proteins and dysregulated pathways for

at this stage, speculative. Some were established in the literature (*e.g.*, the G4-forming sequence found in the promoter region of PCNA and BLM, in the 5′-untranslated region (UTR) of FEN1 mRNA (*vide infra*) for instance) (74, 75), but the existence of G4s related to most of the DEGs/DEPs described above remained to be demonstrated.

To investigate this in detail, we evaluated the G4 content of the mRNA coding the DEPs using G4Hunter, which estimates the probability of G4 formation within a sequence *via* a score (G4H score) (12). From the 107 proteins found to be dysregulated by the two compounds, we selected only the DEPs whose statistical significance was established upon both PDS- and PhpC-treatment ($p \leq 0.01$). This selection led to 58 candidates (Fig. 5*A*), including four $PDS^-/PhpC^-$ (*i.e.*, EIF5, HECTD3, ICMT, MYL10), four $PDS^-/PhpC^+$ (*i.e.*, EIF4A1, MKI67, PRMT5, SEC61B), and 50 $PDS^+/PhpC^+$ proteins (*e.g.*, DDX10, ERCC3). The corresponding mRNA sequences were obtained from the National Center for Biotechnology Information (NCBI) using the reference genome assembly GRCh38.p14 (GCF_000001405.40), were computed to identify their putative quadruplex sequences (PQS). We selected a rather low detection threshold (=1.0 *versus* the classically used 1.5) for two reasons. First, we calibrated our investigations with established RNA G4-forming sequences and found that they display low scores, such as FEN1 (see above, $^{5'}GCAG_2CUCAG_2CUGCUG_4C_2GAGCAG_2AG_2UG_2{}^{3'}$, localization: +449/+511, G4H score = 1.3)) (74). Second, G4 ligands (notably PDS) preferentially stabilize weaker G4s (that is, G4s with an average score centered on *ca*. 1.0) in human cells (76). Using these conditions, we found that the 58 studied mRNAs contain at least one PQS, *i.e.*, 4 to 13 PQSs for $PDS^-/PhpC^-$ DEPs (score ≤ 2.00), 1 to 27 for $PDS^-/PhpC^+$ (score ≤ 2.35), and 1 to 58 for $PDS^+/PhpC^+$ (score ≤ 2.75), which represents a high G4-content, with an average of 9.5 PQS/transcript for $PDS^-/PhpC^-$, 10.5 for $PDS^-/PhpC^+$ and 10.9 for $PDS^+/PhpC^+$ (Fig. 5*B*).

To go a step further, the localization of these PQSs across the different mRNA sections (5′-UTR, coding sequence (CDS), and 3′-UTR) was investigated (Fig. 5, *C* and *D*). In the $PDS^-/PhpC^-$ transcripts, PQSs are mainly located in the 3′-UTR (23 out of 38 PQSs, 61%) *versus* CDS (15 out of 38 PQSs, 39%). In the $PDS^-/PhpC^+$ transcripts, the PQSs are mainly located in CDS (24 out of 42 PQSs, 57%) *versus* 5′-UTR (4 out of 42 PQSs, 10%) and 3′-UTR (14 out of 42 PQSs, 33%); in the $PDS^+/PhpC^+$ transcripts, the PQSs are mainly located in the 3′-UTR (268 out of 546 PQSs, 49%) *versus* CDS (223 out of 546 PQSs, 41%) and 5′-UTR (55 out of 546 PQSs, 10%). This might have consequences in the regulation of mRNA expression. For instance, the transcripts whose expression is upregulated by PhpC tend to have a high G4 content in their CDS (57 *versus* 39% for $PhpC^-$), which is in line with the known ability of these G4s to stall polymerases. They also have PQSs in their 5′-UTR (10 *versus* 0% for $PhpC^-$), which is also consistent with the ability of these G4s to hamper proper mRNA scanning (77). Conversely, those downregulated by PhpC display a high PQS content in the 3′-UTR (61 *versus* 33% for $PhpC^+$), which is in agreement with the influence of these G4s on mRNA stability (78).

Altogether, these *in silico* investigations demonstrated the G4-richness of identified DEGs/DEPs and confirmed their reliability as targets for both PDS and PhpC. To provide an experimental validation, we selected 10 genes for both the good G4Hscore of their PQSs (>1) and the modulation of their expression by PDS/PhpC: ADRA2C, ANKHD1-EIF4EBP3, BORA, ERCC6L, FEN1, ICMT, MKI67, NEFL, NUCKS1, and RILPL1. This selection comprises 7 DNA PQSs detected by RNA-seq, for qPCR validation: ADRA2C (PDS^+ and $PhpC^+$), ANKHD1-EIF4EBP3 (PDS^+ and $PhpC^+$), BORA (PDS^-), ERCC6L (PDS^-), FEN1 (PDS^-), MKI67 (PDS^-) and NEFL ($PhpC^-$); and 7 RNA PQSs detected by MS, for immunoassay validation: BORA (PDS^- and $PhpC^-$), ERCC6L (PDS^-), FEN1 (PDS^+ and $PhpC^+$), ICMT (PDS^- and $PhpC^-$), MKI67 (PDS^- and $PhpC^+$), NUCKS1 (PDS^+ and $PhpC^-$), and RILPL1 (PDS^+ and $PhpC^+$). We selected only 1 PQS per gene/transcript, which represents only a small fraction of the total number of PQS (10 out of 170 PQS, 5.9%; the number of PQS being 15 in ADRA2C, 55 in ANKHD1-EIF4EBP3, six in BORA, nine in ERCC6L, nine in FEN1, 13 in ICMT, 27 in MKI67, 11 in NEFL, 16 in NUCKS1, and nine in RILPL1).

The G4 folding of these PQSs was evaluated by circular dichroism (CD) and thermal difference spectra (TDS) (79), FRET-MC assay (80) and fluorescence titrations (with NMM) (81), and quantified *via* a cumulative score (Fig. 6*A*, and the Supplementary Figs. S10-S16 and Tables S1–S9). We found that 57% (8 out of 14 PQSs) do actually fold into G4s (score >1.5), which is relevant with respect to the very narrow selection of PQSs (*ca*. 6%). We thus translated this into a functional analysis, assessing the PDS-/PhpC-mediated modulation of the corresponding DEGs by quantitative PCR and DEPs by capillary-based immunoassay (Fig. 6, *B* and *C*, and Supplementary Figs. S17–S19 and Table S10): quite remarkably, the results obtained with low-throughput techniques fully matched RNA-seq and MS (Fig. 6*D*), with the exception of NUCKS1 (no reliable antibody) and MKI67 (above the capillary limits). These results thus provide the validation of both the functional relationship between G4s, transcription and translation, and the functional relevance of a G4 ligand-mediated control of gene expression.

Discussion

We performed a comprehensive study of the effects of G4 stabilization by PDS or G4 destabilization by PhpC at the transcriptome- and proteome-wide scales in primary human

PDS^+ treated human astrocytes. *D*, the string protein-protein interaction analysis showing the examples of enrichment maps of proteins and dysregulated pathways for PDS^-. *E*, the string protein-protein interaction analysis shows the examples of enrichment maps of proteins and dysregulated pathways for $PhpC^+$. *F*, the string protein-protein interaction analysis showing the examples of enrichment maps of proteins and dysregulated pathways for $PDS^-/PhpC^-$, $PDS^-/PhpC^+$ and $PDS^+/PhpC^+$ (gene sets: node; gene presence: edge) (see the supplementary data).

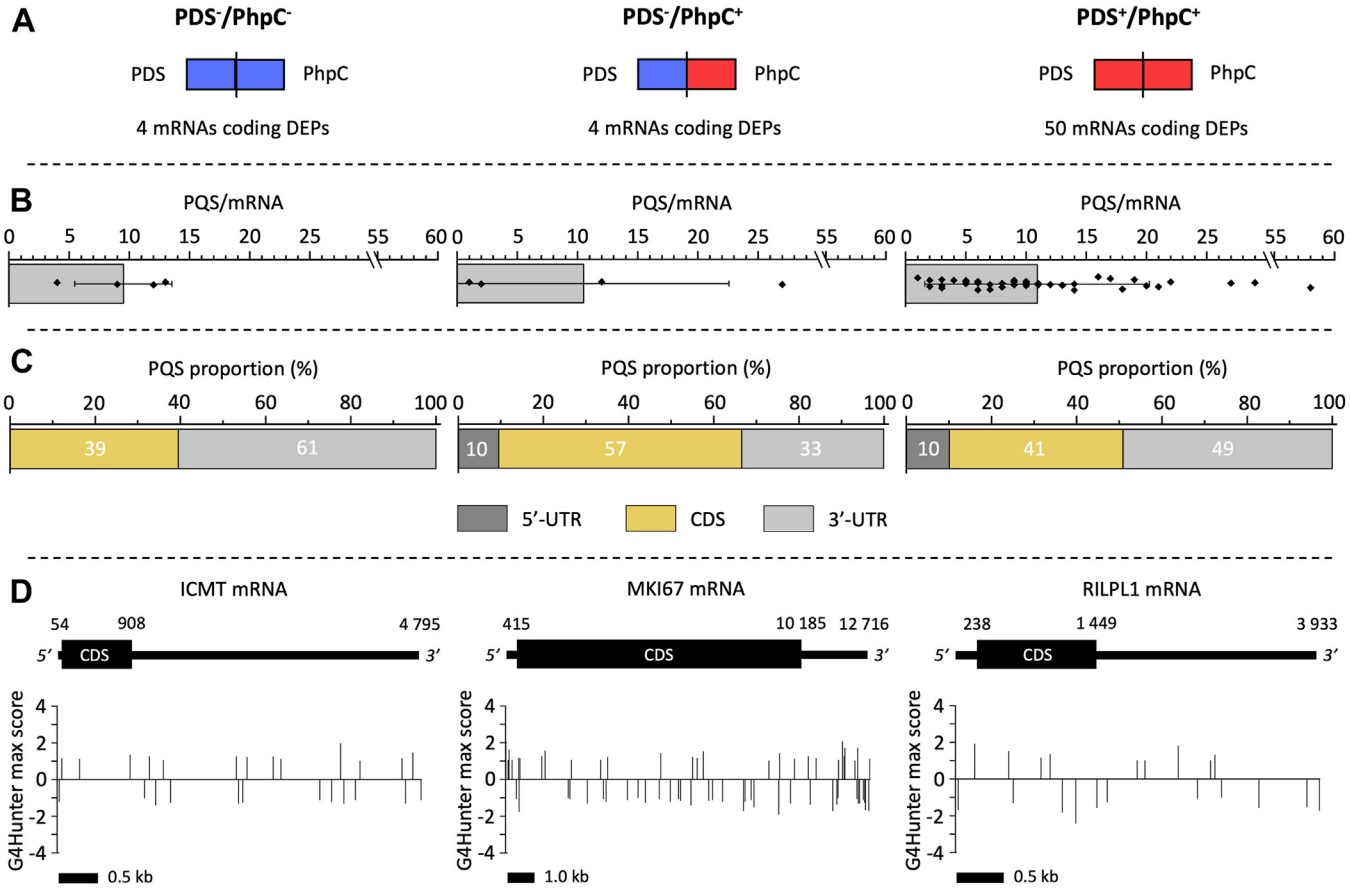

Figure 5. A G4-motif analysis for genes altered by PDS and PhpC in human astrocytes. *A*, G4 content estimation within mRNA coding 58 significant DEPs representing motifs for four PDS⁻/PhpC⁻, four PDS⁻/PhpC⁺ and 50 PDS⁺/PhpC⁺. *B*, schematic representation of the distribution of PQS *per* mRNA using G4hunter. *C*, a diagram showing the distribution of PQS across the various sections of mRNA, 5′UTR, CDS, and 3′UTR. *D*, examples of distribution of PQS across sections of mRNA for genes ICMT, MKI67, and RILPL1.

astrocytes. Our results confirm that, just like in many other cell types (62, 82–85), PDS is a quite active, pan-G4 ligand that affects a broad variety of cellular processes. Its toxicity primarily originates in its inhibitory properties, with the downregulation of 354 transcripts (RNA-seq) and 158 proteins (MS), which affects many different pathways mostly related to RNA transactions. In contrast, PhpC modulates the G4 landscapes in a more focused manner, altering only the translational activity in astrocytes (likely because of a preferential interaction with RNA G4s, previously demonstrated by G4RP) with the upregulation of 295 proteins mostly involved in RNA transactions, thus mirroring the effects of PDS.

From the G4 point of view, the 107 proteins dysregulated by PDS and PhpC offer a unique and dazzling display of the role that G4s play in human astrocytes. Importantly, G4 folding and unfolding do not necessarily correspond to inhibition and activation of cellular processes, respectively. Indeed, depending on the localization of the G4-forming sequence within the gene/transcript (UTR or CDS), G4s promote (behaving as docking sites, for instance) (86–88) or hamper (behaving as an impediment to polymerase motion, for instance) (89–91) the related transactions. Therefore, PDS⁻ and PDS⁺ and, accordingly, PhpC⁻ and PhpC⁺ can be interpreted to cast a light on the involvement of G4s in cellular biology. Among this set of dysregulated proteins, both iPathwayGuide and STRING analyses point toward key G4 roles in the regulation of stress response and protein production and localization, thus confirming the functional prevalence of G4-associated pathways in astrocytes and the relevance of the strategies aiming at targeting G4s to harness the cells' operational pattern.

From a molecular point of view, our results confirm that PDS indiscriminately causes casualties, up- and downregulating gene expression at transcriptional (516 DEGs, 31% up, 69% down) and translational steps (381 DEPs, 58% up, 42% down). These results contribute to nurturing a better understanding of the mechanism by which PDS exerts its antiproliferative activity (46, 82, 84, 85), initially suspected not to be sufficiently controllable for being pushed towards clinical investigations while a recent study shows that it might be considered as a good candidate for further therapeutic developments (92). PhpC behaves in a radically different manner, upregulating gene expression at the translational step only (nine DEGs only *versus* 314 DEPs, 94% up, 6% down). These results thus contribute to unraveling the mechanism of action of PhpC in human cells, which makes it a serious candidate for entering preclinical/clinical trials in light of its good drug-like

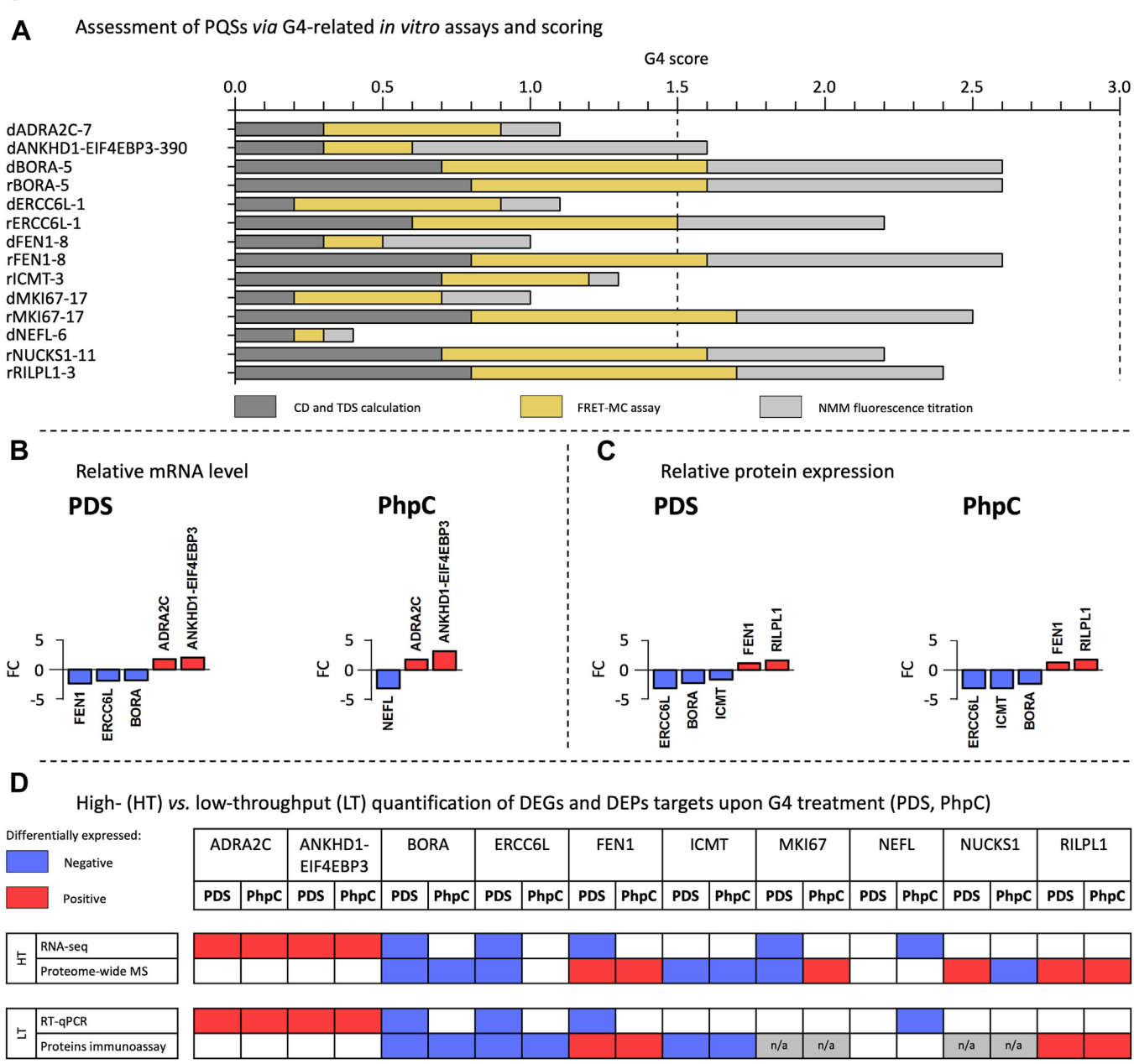

Figure 6. An experimental confirmation of the G4-folding of identified PQSs and G4-mediated modulation of gene expression. *A*, *in vitro* confirmation of the G4-folding of 7 DNA PQSs and 7 RNA PQS corresponding to 10 genes/transcripts whose expression is modulated by PDS/PhpC *via* CD and TDS profiles, FRET-MC investigations and NMM fluorescence titrations (cumulative score, see the Supporting Information for calculation details). *B*, modulation by PDS or PhpC of the cellular level of eight transcripts established by qPCR. *C*, modulation by PDS or PhpC of the cellular level of 10 proteins established by capillary-based immunoassay. *D*, comparison of the G4 ligand-mediated modulation of gene expression established by by high-*versus* low-throughput techniques.

properties (Lipinski's profile) (93) implying advantageous pharmacological properties (small size, high bioavailability, low toxicity). PDS and PhpC might not interact with the same G4s, even within the same gene/transcript, nor with the same affinity. Despite these differences, we found that PhpC triggers effects opposite to PDS, favoring sheltering effects while PDS favors inhibitory effects. PhpC could, therefore, be considered a senolytic drug that may find many applications in designing strategies to prevent G4-associated molecular and genetic dysfunctions associated with age-related neurological disorders.

Experimental procedures

Isolation and culture of primary human astrocytes

In this study, we collected epileptic brain tissue resection from the frontal lobe of a 32-year-old male patient, maintaining sterility throughout the process. The patient had no known pathological conditions or co-morbidities, and ethical standards, including obtaining informed consent, were observed throughout the handling of the human tissue sample. The brain sample was subjected to a 30-s sterilization step using 20% betadine solution, followed by thorough rinsing with 1X PBS.

Subsequently, the tissue was finely diced into 1-mm-sized pieces on a sterile petri dish, and these explants were then transferred to PDL-coated plates and air-dried for 10 min. The explants were cultured in DMEM growth medium supplemented with 10% FBS, as well as antibiotics, penicillin, and streptomycin. After culturing them for 2 to 3 weeks, astrocytes were isolated from the explants and continued their culture in DMEM growth medium enriched with recombinant human TGF-α and human NRG1-β1 growth factors, promoting their maturation and differentiation until 3 to 4 passages.

Immunocytochemistry

Cultured human astrocytes were grown on Geltrex-coated chambered slides and subjected to immunofluorescence staining. After a preliminary wash with 1X phosphate-buffered saline (PBS), the cells were fixed using 4% paraformaldehyde for 10 min at room temperature, followed by PBS washes. Subsequent permeabilization and blocking were done using 5% normal goat serum, 1% bovine serum albumin, and 0.3% Triton-X-100 for 45 min at room temperature. The astrocytes were then incubated with a primary antibody prepared in the blocking solution overnight at 4 °C, washed thrice with PBS for 5 min each, and subsequently incubated with a fluorophore-tagged secondary antibody for 1 h at room temperature. The slides were mounted with a DAPI-containing mounting medium, enabling visualization using fluorescence microscopy.

Fluorescence microscopy and image analyses

Fixed cells were imaged using a Nikon A1R Confocal Laser Microscope, employing 20X, 40X, and 63X objectives. To ensure uniformity and comparability across all samples, imaging parameters, including light intensity, gain, and other relevant settings, were maintained constant throughout the imaging process. Subsequently, the acquired images were analyzed and quantified using ImageJ/Fiji software, enabling standardized measurements and evaluations of the experimental data.

In vitro *maturation of human astrocytes and small molecule treatment for RNA-sequencing and mass spectrometry analysis*

Human astrocytes, isolated from the explants, were cultured *in vitro* in DMEM media supplemented with FBS and growth factors for a minimum of 3 to 4 passages, ensuring their maturation and differentiation. Astrocytes were cultured in PDL-coated T25 flasks at a seeding density of approximately two million cells per flask. Cells were treated with PDS (2 μM) or PhpC (20 μM) for 24 h. The following day, for RNA-sequencing, the cells were lysed in 1 ml of RLT buffer obtained from Qiagen, and for mass spectrometry, cells were collected in 1X PBS. Cells were rapidly frozen and stored at −80 °C until further analysis.

Sample preparation, library preparation, mRNA sequencing, and data analysis workflow

Human astrocytes age 32, male untreated (control), n = 5, or treated with PDS, n = 5, or PhpC, n = 5, were lysed in RTL lysis buffer and freeze for RNA isolation. RNA isolation was performed using the RNeasy Mini kit (Qiagen) and the manufacturer's guidelines, with elution on a 30-μL volume. Subsequent library preparation was carried out adhering to the standard QIAseq stranded mRNA Kit (Qiagen) protocol. Starting with 500 ng of initial material, mRNA was enriched and heat fragmented. After the first- and second-strand synthesis, complementary DNA underwent end-repair and 3′ adenylation. Sequencing adapters were then ligated to the overhangs, and molecules carrying adapters were enriched through 13 cycles of PCR and purified using bead-based cleanup. Library quality control was performed using capillary electrophoresis (Tape D1000), and high-quality libraries were pooled based on equimolar concentrations. The concentration of the library pool was quantified using qPCR, and this optimal concentration was utilized to generate clusters on the surface of a flow cell. Sequencing was conducted on a Nextseq instrument (Illumina Inc.), according to the manufacturer's instructions, producing paired-end reads (2 x 75, 2 x 10). Primary data analysis was carried out using CLC Genomics Server 22.0.02. Initial data processing involved trimming to remove potential read-through adapter sequences at the 3′end, followed by quality score-based trimming and handling of reads containing ambiguous nucleotides (up to two per read). The trimmed reads were first mapped to the human ribosomal RNA (rRNA) repetitive unit to assess the rRNA content in the samples. Subsequently, all reads were mapped to the human genome GRCh38 with ENSEMBL GRCh38 version 98 annotation. For differential expression analysis, the 'empirical analysis of DGE' algorithm within the CLC Genomics Workbench 22.0.2 was employed with default settings, utilizing the 'Exact Test' from the EdgeR Bioconductor package for two-group comparisons. Only genes with at least 10 counts summed across all samples were considered for unsupervised analysis. A variance stabilizing transformation was applied to the raw count matrix using the R package DESeq2 version 1.28.1. The 500 genes with the highest variance were used for the principal component analysis, and the variance values were calculated agnostically to predefined groups (blind = TRUE). Finally, hierarchical clustering was performed using the top 35 genes exhibiting the highest variance across samples.

Sample preparation, library preparation, and mass spectrometry

Human astrocytes age 32, male untreated (control), n = 3, or treated with PDS, n = 3, or PhpC, n = 3, underwent lysis using a solution containing 50 mM ammonium bicarbonate and 1 mM calcium chloride, followed by sonication for 3 min at 30 amp with a 30-s pulse, and a 1-min rest at 4 °C. Protein concentration was determined using the Bradford method, with subsequent digestion of 25 μg of lysate using 0.5 μg of trypsin for 12 h at 37 °C. Tryptic peptide concentration was assessed using the Pierce Quantitative Peptide Assays kit (ThermoFisher Scientific cat# 23275), and 25 μg of peptides were chromatographically separated on a custom-made reverse-phase C18 column within a pipet tip. The eluted

peptides were fractionated into 15 distinct fractions of 150 µl each by employing a stepwise gradient of increasing acetonitrile concentration (ranging from 2 to 35%) at pH 10. Following this, the fractions were amalgamated into five groups by combining different % of acetonitrile eluent (2 + 12 + 22%, 4 + 14 + 24%, 6 + 16 + 26%, 8 + 18 + 28%, 10 + 20 + 35%) and desiccated under vacuum. The resultant dried peptide samples were reconstituted in a solution consisting of 5% methanol and 0.1% formic acid in water, and subsequently subjected to analysis using Orbitrap Fusion mass spectrometers (Thermo Fisher Scientific) in conjunction with an Easy-nLC 1000 nanoflow LC system (Thermo Fisher Scientific). For the analysis, an in-house trap column packed with 1.9-µm Reprosil-Pur Basic C18 beads (2 cm × 100 µm) and a capillary separation column (5 cm × 150 µm) packed with the same beads were employed. Separation was conducted using a 75-min discontinuous gradient of acetonitrile (ranging from 4% to 26%) and 0.1% formic acid, at a flow rate of 800 nl/min. The instrument, controlled by Xcalibur software version 4.1, (Thermo Fisher Scientific) operated in data-dependent mode, acquiring fragmentation spectra of the top three most intense ions. The parent mass spectrum was obtained in the Orbitrap with a full MS range spanning from 300 to 1400 m/z, operating at a resolution of 120,000. Subsequently, higher-energy collisional dissociation (HCD) was employed to fragment the ions, and MS/MS spectra were acquired in the ion trap using rapid scan mode. These MS/MS spectra were then searched against the target-decoy mouse RefSeq database (release March 23, 2020, containing 62,232 entries) within the Proteome Discoverer 2.1 interface utilizing the Mascot algorithm (Mascot 2.4, Matrix Science). A precursor mass tolerance of 20 ppm and a fragment mass tolerance of 0.5 Da were permitted. Additionally, up to two missed cleavages were allowed, and dynamic modifications such as acetylation of N-term and oxidation of methionine were considered. Assigned peptides underwent filtration with a 1% false discovery rate using Percolator validation based on q-value. The Peptide Spectrum Matches obtained from Proteome Discoverer 2.1 were processed using the 'gpGrouper' algorithm to group peptides at the gene level. This in-house program, gpGrouper, employs a universal peptide grouping logic to accurately allocate and provide MS1-based quantification across multiple gene products (94). Quantification of gene-protein products was conducted using the label-free, intensity-based absolute quantification (iBAQ) approach (94). Subsequently, the quantification values were normalized to FOT (Fraction of Total), which represents a fraction of the total protein iBAQ amount per experiment. FOT was calculated as an individual protein's iBAQ divided by the total iBAQ of all identified proteins within a single experiment. This normalization step helps in comparing protein abundances across different samples or experiments.

RNA-sequencing and mass spectrometry data analysis

The RNA sequencing and mass spectrometry data were subjected to analysis using iPathwayGuide, a tool provided by Adviata Bioinformatics. The analysis was performed within the context of pathways sourced from the KEGG (Kyoto Encyclopedia of Genes and Genomes) database, as well as gene ontologies obtained from the GO Consortium database. The analysis integrated these data sources to construct underlying topologies, which represent the network of genes and proteins and their directional interactions. The topologies were derived from the KEGG database utilizing iPathwayGuide, providing valuable insights into the biological pathways and processes influenced by the differential gene expression patterns identified through RNA sequencing and mass spectrometry. These data are gathered in Supplementary Files S1 and S2.

String analysis

Functional network analysis was performed using STRING (https://string-db.org/) for six families of differently expressed proteins extracted from the iPathwayGuide (Advaita Bioinformatics) protein lists provided in the Supplementary File 3 (*i.e.*, 223 PDS^+, 295 $PhpC^+$, 5 $PDS^-/PhpC^-$, 9 $PDS^-/PhpC^+$ and 92 $PDS^+/PhpC^+$ proteins) using *Homo sapiens* organism, full STRING network, evidence network edges, medium confidence interaction score (0.400) and confidence strength (s) ≥ 0.70 within Biological Process (Gene Ontology) as outputs.

G4 motif analysis using G4Hunter

G4Hunter scores were computed using specific parameters: information (length in base, genomic subdomains (UTRs and CDS) positions) and FASTA files of mRNAs (real variant 1, regardless of the number of real and predicted mRNA or ncRNA variants) coding DEPs were first extracted from the reference genome assembly GRCh38.p14 (GCF_000001405.40) *via* the NCBI database and then processed through the dedicated G4Hunter website (https://g4hunter.shinyapps.io/G4HunterMultiFastaSeeker/) with a window of 20 and a minimal score (threshold) of 1.0. Each 'hit' (or putative G-quadruplex sequence, PQS) is characterized by its genomic coordinates and a 'max_score' reflecting the score of the highest G4Hunter within this window. These data are available in the Supplementary File 4. The number of PQS per genomic subdomains for each significant common DEPs groups ($PDS^-/PhpC^-$, $PDS^-/PhpC^+$, and $PDS^+/PhpC^+$) was gathered manually, analyzed with Excel (Microsoft Corp.) and OriginPro (OriginLab Corporation).

G4-interacting molecules

PDS (Sigma-Aldrich, cat. n° SML2690), Phen-DC_3 (Sigma-Aldrich, cat. n° SML2298), and N-TASQ (lab made) were solubilized at 5, 1, and 20 mM, respectively, in ultrapure water and stored at −20 °C. NMM (Cayman Chemical, cat. n° 27,210) was solubilized at 10 mM in DMSO and stored at −80 °C.

Oligonucleotides

All oligonucleotides (ONs) used here (Supplementary information) were purchased from Eurogentec (Seraing,

Belgium), diluted in ultrapure water (18.2 MΩ.cm resistivity) at 500 μM for stock solutions and stored at −20 °C. The actual concentration of these stock solutions was determined through a dilution to 5 μM theoretical concentration *via* a UV spectral analysis at 260 nm with the molar extinction coefficient values provided by the manufacturer. F21T was prepared at 25 μM in a CacoK10 buffer (10 mM lithium cacodylate buffer pH 7.2, 10 mM KCl, 90 mM LiCl). The other ONs were prepared at 50 μM in three different buffers: CacoK10, CacoNa10 (10 mM lithium cacodylate buffer pH 7.2, 10 mM NaCl, 90 mM LiCl) or CacoLi100 buffer (10 mM lithium cacodylate buffer pH 7.2, 100 mM LiCl). The (possible) high-order structure was folded by heating the previously prepared solution at 90 °C for 5 min, cooling it on ice (<1 h) and then storing it at least overnight at 4 °C.

Circular dichroism (CD) and Absorbance (Abs) measure, and thermal difference signature (TDS) calculation

All ONs were dissolved at a concentration of 3 μM (final volume = 100 μl) in CacoK10, CacoNa10, or CacoLi100 buffer according to the buffer used for their stock preparation (see above). Mineral oil (300 μl; ThermoFisher, cat. n° 415,080,010) was added on top of the 100 μl samples to avoid evaporation. The experiments were performed in a quartz semi-micro cuvette (Starna) with a path length of 10 mm on a Jasco J-815 spectropolarimeter. Data were recorded from 350 to 210 nm, at a rate of 200 nm per min with a 1 s response time, 1 nm pitch, 1 nm bandwidth, and are an average of two scans. The CD and Abs spectra were recorded at 25 °C and 95 °C (then, data were zeroed at 350 nm). Thermal difference signature (TDS) spectra were obtained by subtracting the 25 °C zeroed Abs spectrum from the 95 °C zeroed Abs spectrum (95 °C − 25 °C) (1). Final data were analyzed with OriginPro, Version 2018 (OriginLab Corporation).

FRET-MC assay

Diluted solutions of G4-interacting molecules (PDS, Phen-DC_3, N-TASQ) at 100 μM were prepared by diluting them with CacoK10 buffer (10 mM lithium cacodylate buffer pH 7.2, 10 mM KCl, 90 mM LiCl). Experiments were performed in 96-well plates using an Mx3005P qPCR device (Agilent) equipped with FAM filters (λ exc = 492 nm; λ em = 516 nm). To a mixture of F21T (final concentration: 0.2 μM) and CacoK10 buffer were added 2 mol. equiv. (*i.e.*, 0.4 μM) of G4-interacting molecule. For competition, to that previous mixture were added 15 mol. equiv (compared to F21T, *i.e.*, 3 μM). of nucleic acid competitors. After an initial equilibration step (25 °C, 30 s), a stepwise increase (1 °C every 30 s for 67 cycles, from 25 to 90 °C) was performed, and measurements were made after each cycle. Final data, from three independent experiments, were analyzed with Excel (Microsoft Corp.) and OriginPro Version 2018 (OriginLab Corporation). The emission of FAM was normalized (0–1) and the $T_{1/2}$ (°C), *i.e.,* the temperature for which the normalized emission is 0.5, was recovered manually. $DT_{1/2}$ (°C) = $T_{1/2}$ (F21T + G4-interacting molecule ± Competitor) − $T_{1/2}$ (F21T). S Factor = $\Delta T_{1/2}$ (F21T + G4-interacting molecule + Competitor)/$\Delta T_{1/2}$ (F21T + G4-interacting molecule). The S Factor gives information about the structure of a nucleic acids sequence: G4 structure (S = 0.0) or not (S = 1.0).

Fluorescence titration

Diluted solutions of G4 probes (N-TASQ, NMM) at 100 μM were prepared by diluting them with CacoK10 buffer (10 mM lithium cacodylate buffer pH 7.2, 10 mM KCl, 90 mM LiCl). Experiments were performed in 96-well plates (chimney well, flat bottom, black plate; Greiner Bio-One cat. n° 655,090) at 25 °C using CLARIOstar plate-reader device (BMG LABTECH). Data were recorded on top of the wells with 50 flashes, 1500 gain, 5 mm focal height, 0.1 s time exposure, and different excitation/emission parameters depending on the G4 probe: N-TASQ (λ_{exc} = 280 nm; λ_{em} = 380–480 nm) or NMM (λ_{exc} = 280 nm; λ_{em} = 540–740 nm). To a mixture of G4 probe (final concentration: 10 μM) and CacoK10 buffer was added 0.3 mol. equiv. (*i.e.*, 3 μM) of ONs. Final data, from three independent experiments, were analyzed with Excel (Microsoft Corp.) and OriginPro Version 2018 (OriginLab Corporation). The emission peak at 414 nm (for N-TASQ) or 610 nm (for NMM) was recovered for Fold change calculation. Fold change = emission peak (sequence + G4 probe)/mean emission peak (G4 probe).

Real-time qPCR

Human astrocytes were treated with PDS (2 μM) or PhpC (20 μM) for 24 h. The following day, the cells were lysed in RLT buffer obtained from Qiagen for RNA isolation. Total RNA was extracted using the RNeasy Mini kit (Qiagen; catalog no: 74,104). 1 μg of RNA was used to prepare the cDNA using iScript Reverse Transcription SuperMix (Bio-Rad; catalog no: 1708840), according to the manufacturer's protocol. Real-time qPCR was performed using Bio-Rad CFX96 machine using SSoAdvanced Universal SYBR Green (Bio-Rad; catalog no:1725275) for visualization and quantification according to the manufacturer's instruction. Primer sequences were mentioned in the Supplementary information. PCR conditions used were: 95 °C for 3 min, followed by 40 cycles of 95 °C for 10 s, and 60 °C for 30 s. TATA-binding protein (TBP) mRNA levels were used as an internal control for the target mRNAs. Normalization and relative fold change expression levels of all genes were calculated from the average threshold cycle number using the delta-delta Ct method.

Capillary-based immunoassay via *ProteinSimple*

The capillary electrophoresis immunoassay was conducted using the JESS Automated Western Blot System (Catalog No. 004–650, ProteinSimple, Bio-techne) to analyze total protein lysates from human astrocytes treated with PDS and PhpC. The lysates were extracted using RIPA lysis buffer (Catalog No. 20–188, EMD Millipore) supplemented with a Protease and Phosphatase inhibitor cocktail (Catalog No. 5872, Cell Signaling Technology), followed by centrifugation at 12,000 rpm for 10 min at 4 °C. Total protein concentration

was determined *via* BCA assay, and samples were diluted in sample buffer (ProteinSimple, Bio-techne) to achieve a final concentration of 1 μg/μl. A master mix (4:1 ratio of protein to master mix) containing a 40 mM fluorescent molecular weight marker with dithiothreitol was prepared, and samples were denatured at 95 °C for 5 min before loading. The proteins were separated in a 25-well plate and capillary for sizes ranging from 12 to 230 kDa. Antibodies were diluted in an antibody diluent (ProteinSimple, Bio-techne) as follows: ICMT (1:50, Catalog No. PA5-85576, ThermoFisher Scientific), FEN1 (1:100, Catalog No. 14768-1-AP, ThermoFisher Scientific), BORA (1:50, Catalog No. 702148, ThermoFisher Scientific), RILPL1 (1:100, Catalog No. MJF-R41–21, Abcam), and ERCC6L (1:100, Catalog No. 15688-1-AP, ThermoFisher Scientific), with detection performed using an HRP-conjugated secondary anti-rabbit antibody. Data analysis involved quantifying relative protein levels through the areas under the peaks from chemiluminescence chromatograms using Compass for SW software (version 6.3.0, ProteinSimple, Bio-techne), with protein values expressed as peak intensity normalized to total protein loading control.

Ethical approval

Human brain tissue samples were obtained and handled in strict adherence to the guidelines and regulations established by the University of Texas, McGovern Medical School at Houston. Ethical considerations and prior consent from the patients were obtained and approved to enable research involving the use of their brain tissue. All experimental protocols underwent approval by the University of Texas, McGovern Medical School at Houston, and the research procedures were conducted in full compliance with the approved guidelines, ensuring ethical and scientific standards throughout the study.

Data availability

The data discussed in this publication have been deposited in NCBI's Gene Expression Omnibus (Edgar *et al.,* 2022) and are accessible through GEO Series accession number GSE279752 (https://www.ncbi.nlm.nih.gov/geo/query/acc.cgi?acc=GSE279752). The mass spectrometry data for proteome profiling have been submitted *via* the MASSIVE repository (MSV000096114) to the ProteomeXchange Consortium (http://proteomecentral.proteomeexchange.org) with the dataset identifier PXD056881.

Supporting information—This article contains supporting information (79, 95–108).

Acknowledgments—We thank members of the A. S. T. laboratory and the BRAINS laboratory for useful discussions. We also thank Suresh Kumar (bioinformatics scientist, Advaita Bioinformatics) for their helpful discussions. Danielle Guillory provided administrative assistance. We also thank Laurent Lacroix for helpful discussions about G4Hunter.

Author contributions—S. Y. J., R. H. E. H., D. M., A. S. T., V. K. M. J., J. M., Z. W., E. W., and N. T. validation; S. Y. J., R. H. E. H., D. M., A. S. T., V. K. M. J., and J. M. investigation; S. Y. J., V. K. M. J., J. M., and Z. W. formal analysis; R. H. E. H, D. M., V. K. M. J., and J. M. supervision; D. M., A. S. T., V. K. M. J., and J. M. writing–review & editing; D. M., A. S. T., V. K. M. J., and J. M. writing–original draft; D. M., A. S. T., V. K. M. J., and J. M. visualization; D. M., V. K. M. J., and J. M. software; D. M., V. K. M. J., and J. M. resources; D. M., A. S. T., V. K. M. J., and J. M. project administration; D. M., A. S. T., V. K. M. J., J. M., E. W., and N. T. methodology; D. M. and A. S. T. funding acquisition; D. M., A. S. T., V. K. M. J., and J. M. data curation; D. M., A. S. T., V. K. M. J., and J. M. conceptualization.

Funding and additional information—This work was supported by the Glenn Foundation and the American Federation for Aging Research (grant ID: BIG21042) to A. S. T., and by the Ligue nationale contre le cancer (grant ID: AAPEAC2022.LCC/VG) and the Glenn Foundation, United States; American Federation for Aging Research, United States; Ligue nationale contre le cancer, France; Centre national de la recherche scientifique, France; Texas Alzheimer's Research and Care Consortium, United States; (CNRS) to D. M. and Postdoctoral Fellowship Grant from Texas Alzheimer's Research and Care Consortium (TARCC – grant ID: 1285130) to V. K. M. J.

Conflict of interest—The authors declare no conflict of interest with the content of the article.

Abbreviations:—The abbreviations used are: CD, circular dichroism; CDS, coding DNA sequence; G4, G-quadruplex; PDS, pyridostatin; Phpc, phenylpyrrolocytosine; G4RP, G4-RNA-specific affinity precipitation; DEGs, differentially expressed genes; DEPs, differentially expressed proteins; GO, Gene Ontology; KEGG, Kyoto Encyclopedia of Genes and Genomes; MS, mass spectrometry; ON, oligonucleotides; PQS, putative quadruplex sequence; qPCR, quantitative (or real time) polymerase chain reaction; RNA-seq, RNA sequencing; TDS, thermal difference spectra; UTR, untranslated region.

References

1. Pauling, L., and Beadle, G. W. (1954) Chemical biology. *Eng. Sci.* **17**, 9–13
2. Schreiber, S. L. (2005) Small molecules: the missing link in the central dogma. *Nat. Chem. Biol.* **1**, 64
3. Altmann, K., Müller, K., Nolan, E. M., Samori, B., Schneider, G., Schreiber, S. L., Schwalbe, H., *et al.* (2009) The state of the art of chemical biology. *ChemBioChem* **10**, 16–29
4. Spiegel, J., Adhikari, S., and Balasubramanian, S. (2020) The structure and function of DNA G-quadruplexes. *Trends Chem.* **2**, 123–136
5. Dumas, L., Herviou, P., Dassi, E., Cammas, A., and Millevoi, S. G. (2021) Quadruplexes in RNA biology: recent advances and future directions. *Trends Biochem. Sci.* **46**, 270–283
6. Varshney, D., Spiegel, J., Zyner, K., Tannahill, D., and Balasubramanian, S. (2020) The regulation and functions of DNA and RNA G-quadruplexes. *Nat. Rev. Mol. Cell Biol.* **21**, 459–474
7. Lyu, K., Chow, E. Y. C., Mou, X., Chan, T. F., and Kwok, C. K. (2021) RNA G-quadruplexes (rG4s): genomics and biological functions. *Nucleic Acids Res.* **49**, 5426–5450
8. Raguseo, F., Chowdhury, S., Minard, A., and Di Antonio, M. (2020) Chemical-biology approaches to probe DNA and RNA G-quadruplex structures in the genome. *Chem. Commun.* **56**, 1317–1324
9. Stefan, L., and Monchaud, D. (2019) Applications of guanine quartets in nanotechnology and chemical biology. *Nat. Rev. Chem.* **3**, 650–668
10. Cammas, A., and Millevoi, S. (2017) RNA G-quadruplexes: emerging mechanisms in disease. *Nucleic Acids Res.* **45**, 1584–1595

11. Ganser, L. R., Kelly, M. L., Herschlag, D., and Al-Hashimi, H. M. (2019) The roles of structural dynamics in the cellular functions of RNAs. *Nat. Rev. Mol. Cell Biol.* **474-489**
12. Bedrat, A., Lacroix, L., and Mergny, J. L. (2016) Re-evaluation of G-quadruplex propensity with G4Hunter. *Nucleic Acids Res.* **44**, 1746–1759
13. Vannutelli, A., Belhamiti, S., Garant, J. M., Ouangraoua, A., and Perreault, J. P. (2020) Where are G-quadruplexes located in the human transcriptome? *NAR Genomics and Bioinformatics* **2**, lqaa035
14. Meier-Stephenson, V. (2022) G4-quadruplex-binding proteins: review and insights into selectivity. *Biophys. Rev.* **14**, 635–654
15. Brosh, R. M., and Matson, S. W. (2020) History of DNA helicases. *Genes* **11**, 255
16. Lerner, L. K., and Sale, J. E. (2019) Replication of G quadruplex DNA. *Genes* **10**, 95
17. Lejault, P., Mitteaux, J., Rota Sperti, F., and Monchaud, D. (2021) How to untie G-quadruplex knots and why? *Cell Chem. Biol.* **28**, 436–455
18. Antcliff, A., McCullough, L. D., and Tsvetkov, A. S. (2021) G-Quadruplexes and the DNA/RNA helicase DHX36 in health, disease, and aging. *Aging (Albany NY)* **13**, 25578
19. Vijay Kumar, M. J., Morales, R., and Tsvetkov, A. S. (2023) G-quadruplexes and associated proteins in aging and Alzheimer's disease. *Front Aging* **4**, 1164057
20. Neidle, S. (2016) Quadruplex nucleic acids as novel therapeutic targets. *J. Med. Chem.* **59**, 5987–6011
21. Monchaud, D. (2020) Annual Reports in Medicinal Chemistry. In: Neidle, S., ed.**, 54**. *The review "Quadruplex detection in human cells"*, Elsevier, Amsterdam, Netherlands: 133–160
22. Robinson, J., Raguseo, F., Nuccio, S. P., Liano, D., and Di Antonio, M. (2021) DNA G-quadruplex structures: more than simple roadblocks to transcription? *Nucleic Acids Res.* **49**, 8419–8431
23. Kosiol, N., Juranek, S., Brossart, P., Heine, A., and Paeschke, K. (2021) G-quadruplexes: a promising target for cancer therapy. *Mol. Cancer* **20**, 40
24. del Mundo, I. M., Vasquez, K. M., and Wang, G. (2019) Modulation of DNA structure formation using small molecules. *Biochim. Biophys. Acta Mol. Cell Res.* **1866**, 118539
25. Weisman-Shomer, P., Cohen, E., Hershco, I., Khateb, S., Wolfovitz-Barchad, O., Hurley, L. H., and Fry, M. (2003) The cationic porphyrin TMPyP4 destabilizes the tetraplex form of the fragile X syndrome expanded sequence d (CGG) n. *Nucleic Acids Res.* **31**, 3963–3970
26. Waller, Z. A. E., Sewitz, S. A., Hsu, S. T. D., and Balasubramanian, S. (2009) A small molecule that disrupts G-quadruplex DNA structure and enhances gene expression. *J. Am. Chem. Soc.* **131**, 12628–12633
27. Zamiri, B., Reddy, K., Macgregor, R. B., and Pearson, C. E. (2014) TMPyP4 porphyrin distorts RNA G-quadruplex structures of the disease-associated r (GGGGCC) n repeat of the C9orf72 gene and blocks interaction of RNA-binding proteins. *J. Biol. Chem.* **289**, 4653–4659
28. Kaluzhny, D., Ilyinsky, N., Shchekotikhin, A., Sinkevich, Y., Tsvetkov, P. O., Tsvetkov, V., *et al.* (2011) Disordering of human telomeric G-quadruplex with novel antiproliferative anthrathiophenedione. *PLoS One* **6**, e27151
29. Mitteaux, J., Lejault, P., Wojciechowski, F., Joubert, A., Boudon, J., Desbois, N., *et al.* (2021) Identifying G-quadruplex-DNA-disrupting small molecules. *J. Am. Chem. Soc.* **143**, 12567–12577
30. Chowdhury, S., Wang, J., Nuccio, S. P., Mao, H., and Di Antonio, M. (2022) Short LNA-modified oligonucleotide probes as efficient disruptors of DNA G-quadruplexes. *Nucleic Acids Res.* **50**, 7247–7259
31. Mitteaux, J., Raevens, S., Wang, Z., Pirrotta, M., Valverde, I. E., Hudson, R. H. E., and Monchaud, D. (2024) PhpC modulates G-quadruplex-RNA landscapes in human cells. *Chem. Commun.* **60**, 424–427
32. Yang, S. Y., Monchaud, D., and Wong, J. M. Y. (2022) Global mapping of RNA G-quadruplexes (G4-RNAs) using G4RP-seq. *Nat. Protoc.* **17**, 870–889
33. Moruno-Manchon, J. F., Lejault, P., Wang, Y., McCauley, B., Honarpisheh, P., Morales Scheihing, D. A., *et al.* (2020) Small-molecule G-quadruplex stabilizers reveal a novel pathway of autophagy regulation in neurons. *eLife* **9**, e52283
34. Rodriguez, R., Müller, S., Yeoman, J. A., Trentesaux, C., Riou, J. F., and Balasubramanian, S. (2008) A novel small molecule that alters shelterin integrity and triggers a DNA-damage response at telomeres. *J. Am. Chem. Soc.* **130**, 15758
35. Moruno-Manchon, J. F., Koellhoffer, E. C., Gopakumar, J., Hambarde, S., Kim, N., McCullough, L. D., and Tsvetkov, A. S. (2017) The G-quadruplex DNA stabilizing drug pyridostatin promotes DNA damage and downregulates transcription of Brca1 in neurons. *Aging (Albany NY)* **9**, 1957
36. Tabor, N., Ngwa, C., Mitteaux, J., Meyer, M. D., Moruno-Manchon, J. F., Zhu, L., *et al.* (2021) Differential responses of neurons, astrocytes, and microglia to G-quadruplex stabilization. *Aging* **13**, 15917–15941
37. Escarcega, R. D., Patil, A. A., Moruno-Manchon, J. F., Urayama, A., Marrelli, S. P., Kim, N., *et al.* (2023) Pirh2-dependent DNA damage in neurons induced by the G-quadruplex ligand pyridostatin. *J. Biol. Chem.* **299**, 105157
38. Scheibye-Knudsen, M., Tseng, A., Borch Jensen, M., Scheibye-Alsing, K., Fang, E. F., Iyama, T., *et al.* (2016) Cockayne syndrome group A and B proteins converge on transcription-linked resolution of non-B DNA. *Proc. Natl. Acad. Sci. U S A.* **113**, 12502–12507
39. Lee, J.-H., Kim, E. W., Croteau, D. L., and Bohr, V. A. (2020) Heterochromatin: an epigenetic point of view in aging. *Exp. Mol. Med.* **52**, 1466–1474
40. Sen, P., Shah, P. P., Nativio, R., and Berger, S. L. (2016) Epigenetic mechanisms of longevity and aging. *Cell* **166**, 822–839
41. Saul, D., and Kosinsky, R. L. (2021) Epigenetics of aging and aging-associated diseases. *Int. J. Mol. Sci.* **22**, 401
42. Tsurumi, A., and Li, W. X. (2012) Global heterochromatin loss: a unifying theory of aging? *Epigenetics* **7**, 1–9
43. Wang, E., Thombre, R., Shah, Y., Latanich, R., and Wang, J. (2021) G-Quadruplexes as pathogenic drivers in neurodegenerative disorders. *Nucleic Acids Res.* **49**, 4816–4830
44. Cave, J. W., and Willis, D. E. (2022) G-quadruplex regulation of neural gene expression. *FEBS J.* **289**, 3284–3303
45. Mueller, S., Sanders, D. A., Di Antonio, M., Matsis, S., Riou, J. F., Rodriguez, R., *et al.* (2012) Pyridostatin analogues promote telomere dysfunction and long-term growth inhibition in human cancer cells. *Org. Biomol. Chem.* **10**, 6537–6546
46. Rodriguez, R., Miller, K. M., Forment, J. V., Bradshaw, C. R., Nikan, M., Britton, S., *et al.* (2012) Small-molecule-induced DNA damage identifies alternative DNA structures in human genes. *Nat. Chem. Biol.* **8**, 301–310
47. Chambers, V. S., Marsico, G., Boutell, J. M., Di Antonio, M., Smith, G. P., and Balasubramanian, S. (2015) High-throughput sequencing of DNA G-quadruplex structures in the human genome. *Nat. Biotechnol.* **33**, 877–881
48. Kwok, C. K., Marsico, G., Sahakyan, A. B., Chambers, V. S., and Balasubramanian, S. (2016) rG4-seq reveals widespread formation of G-quadruplex structures in the human transcriptome. *Nat. Meth.* **13**, 841–844
49. De Magis, A., Limmer, M., Mudiyam, V., Monchaud, D., Juranek, S., and Paeschke, K. (2023) UV-induced G4 DNA structures recruit ZRF1 which prevents UV-induced senescence. *Nat. Commun.* **14**, 6705
50. Teng, X., Hu, D., Dai, Y., Jing, H., Hu, W., Zhang, Q., *et al.* (2024) Discovery of A G-Quadruplex unwinder that unleashes the translation of G-quadruplex-containing mRNA without inducing DNA damage. *Angew. Chem. Int. Ed.* **63**, e202407353
51. Nicoletto, G., Terreri, M., Maurizio, I., Ruggiero, E., Cernilogar, F. M., Vaine, C. A., *et al.* (2024) G-quadruplexes in an SVA retrotransposon cause aberrant TAF1 gene expression in X-linked dystonia parkinsonism. *Nucleic Acids Res.* **52**, 11571–11586
52. Jakel, S., and Dimou, L. (2017) Glial cells and their function in the adult brain: a journey through the history of their ablation. *Front Cell Neurosci* **11**, 24
53. Acioglu, C., Li, L., and Elkabes, S. (2021) Contribution of astrocytes to neuropathology of neurodegenerative diseases. *Brain Res.* **1758**, 147291
54. Brandebura, A. N., Paumier, A., Onur, T. S., and Allen, N. J. (2023) Astrocyte contribution to dysfunction, risk and progression in neurodegenerative disorders. *Nat. Rev. Neurosci.* **24**, 23–39

55. Phatnani, H., and Maniatis, T. (2015) Astrocytes in neurodegenerative disease. *Cold Spring Harbor Persp. Biol.* **7**, a020628
56. Palmer, A. L., and Ousman, S. S. (2018) Astrocytes and aging. *Front. Aging Neurosci.* **10**, 337
57. Hol, E. M., and Pekny, M. (2015) Glial fibrillary acidic protein (GFAP) and the astrocyte intermediate filament system in diseases of the central nervous system. *Curr. Opin. Cell Biol.* **32**, 121–130
58. Papadopoulos, M. C., and Verkman, A. S. (2013) Aquaporin water channels in the nervous system. *Nat. Rev. Neurosci.* **14**, 265–277
59. Kim, K., Lee, S. G., Kegelman, T. P., Su, Z. Z., Das, S. K., Dash, R., *et al.* (2011) Role of excitatory amino acid transporter-2 (EAAT2) and glutamate in neurodegeneration: opportunities for developing novel therapeutics. *J. Cell. Physiol.* **226**, 2484–2493
60. Cristóvão, J. S., and Gomes, C. M. (2019) S100 proteins in Alzheimer's disease. *Front. Neurosci.* **13**, 463
61. Chen, K.-Z., Liu, S. X., Li, Y. W., He, T., Zhao, J., Wang, T., *et al.* (2023) Vimentin as a potential target for diverse nervous system diseases. *Neural Regen. Res.* **18**, 969–975
62. Miglietta, G., Russo, M., Duardo, R. C., and Capranico, G. (2021) G-quadruplex binders as cytostatic modulators of innate immune genes in cancer cells. *Nucleic Acids Res.* **49**, 6673–6686
63. Kanehisa, M., Furumichi, M., Tanabe, M., Sato, Y., and Morishima, K. (2016) KEGG: new perspectives on genomes, pathways, diseases and drugs. *Nucleic Acids Res.* **45**, D353–D361
64. Ashburner, M., Ball, C. A., Blake, J. A., Botstein, D., Butler, H., Cherry, J. M., *et al.* (2000) Gene Ontology: tool for the unification of biology. *Nat. Genet.* **25**, 25–29
65. Consortium, T. G. O., Balhoff, J., Carbon, S., Cherry, J. M., Drabkin, H. J., Ebert, D., *et al.* (2023) The gene Ontology knowledgebase in 2023. *Genetics* **224**, iyad031
66. Ahsan, S., and Drăghici, S. (2017) Identifying significantly impacted pathways and putative mechanisms with iPathwayGuide. *Curr. Protoc. Bioinformatics* **57**, 7.15.11–17.15.30
67. Rota Sperti, F., Dupouy, B., Mitteaux, J., Pipier, A., Pirrotta, M., Chéron, N., *et al.* (2022) Click-chemistry-based Biomimetic ligands efficiently capture G-quadruplexes in vitro and help localize them at DNA damage sites in human cells. *JACS Au* **2**, 1588–1595
68. Blackford, A. N., and Jackson, S. P. (2017) ATM, ATR, and DNA-PK: the trinity at the heart of the DNA damage response. *Mol. Cell* **66**, 801–817
69. Szklarczyk, D., Franceschini, A., Wyder, S., Forslund, K., Heller, D., Huerta-Cepas, J., *et al.* (2014) STRING v10: protein–protein interaction networks, integrated over the tree of life. *Nucleic Acids Res.* **43**, D447–D452
70. Jia, L., Mao, Y., Ji, Q., Dersh, D., Yewdell, J. W., and Qian, S. B. (2020) Decoding mRNA translatability and stability from the 5′ UTR. *Nat. Struct. Mol. Biol.* **27**, 814–821
71. Turner, M., Danino, Y. M., Barshai, M., Yacovzada, N. S., Cohen, Y., Olender, T., *et al.* (2022) rG4detector, a novel RNA G-quadruplex predictor, uncovers their impact on stress granule formation. *Nucleic Acids Res.* **50**, 11426–11441
72. Kharel, P., and Ivanov, P. (2015) RNA G-quadruplexes and stress: emerging mechanisms and functions. *Trends Cell Biol* **34**, 771–784
73. Rhodes, D., and Lipps, H. J. (2015) G-quadruplexes and their regulatory roles in biology. *Nucleic Acids Res.* **43**, 8627–8637
74. Ma, N., Yang, Y., Xin, J., He, L., Hu, Z., Gao, T., *et al.* (2023) RNA G-quadruplex within the 5'-UTR of FEN1 regulates mRNA stability under oxidative stress. *Antioxidants* **12**, 276
75. Fleming, A. M., Zhu, J., Ding, Y., Visser, J. A., Zhu, J., and Burrows, C. J. (2018) Human DNA repair genes possess potential G-quadruplex sequences in their promoters and 5′-untranslated regions. *Biochem.* **57**, 991–1002
76. Esnault, C., Magat, T., Zine El Aabidine, A., Garcia-Oliver, E., Cucchiarini, A., Bouchouika, S., *et al.* (2023) G4access identifies G-quadruplexes and their associations with open chromatin and imprinting control regions. *Nat. Genet.* **55**, 1359–1369
77. Leppek, K., Das, R., and Barna, M. (2018) Functional 5′ UTR mRNA structures in eukaryotic translation regulation and how to find them. *Nat. Rev. Mol. Cell Biol.* **19**, 158–174
78. Beaudoin, J. D., and Perreault, J. P. (2013) Exploring mRNA 3′-UTR G-quadruplexes: evidence of roles in both alternative polyadenylation and mRNA shortening. *Nucleic Acids Res.* **41**, 5898–5911
79. Mergny, J. L., Li, J., Lacroix, L., Amrane, S., and Chaires, J. B. (2005) Thermal difference spectra: a specific signature for nucleic acid structures. *Nucleic Acids Res.* **33**. e138–e138
80. Luo, Y., Granzhan, A., Verga, D., and Mergny, J. L. (2021) FRET-MC: a fluorescence melting competition assay for studying G4 structures in vitro. *Biopolymers* **112**, e23415
81. Sabharwal, N. C., Savikhin, V., Turek-Herman, J. R., Nicoludis, J. M., Szalai, V. A., and Yatsunyk, L. A. (2014) N-methylmesoporphyrin IX fluorescence as a reporter of strand orientation in guanine quadruplexes. *FEBS J.* **281**, 1726–1737
82. Zimmer, J., Tacconi, E. M. C., Folio, C., Badie, S., Porru, M., Klare, K., *et al.* (2016) Targeting BRCA1 and BRCA2 Deficiencies with G-quadruplex-interacting compounds. *Mol. Cell* **61**, 449–460
83. Zyner, K. G., Mulhearn, D. S., Adhikari, S., Martínez Cuesta, S., Di Antonio, M., Erard, N., *et al.* (2019) Genetic interactions of G-quadruplexes in humans. *eLife* **8**, e46793
84. Olivieri, M., *et al.* (2020) A genetic map of the response to DNA damage in human cells. *Cell* **182**, 481–496.e421
85. Bossaert, M., Pipier, A., Riou, J. F., Noirot, C., Nguyên, L. T., Serre, R. F., *et al.* (2021) Transcription-associated topoisomerase 2α (TOP2A) activity is a major effector of cytotoxicity induced by G-quadruplex ligands. *eLife* **10**, e65184
86. Spiegel, J., Cuesta, S. M., Adhikari, S., Hänsel-Hertsch, R., Tannahill, D., and Balasubramanian, S. (2021) G-quadruplexes are transcription factor binding hubs in human chromatin. *Genome Biol.* **22**, 117
87. Esain-Garcia, I., Kirchner, A., Melidis, L., Tavares, R.d. C. A., Dhir, S., Simeone, A., *et al.* (2024) G-quadruplex DNA structure is a positive regulator of *MYC* transcription. *Proc. Natl. Acad. Sci. U S A.* **121**, e2320240121
88. Song, J., Perreault, J.-P., Topisirovic, I., and Richard, S. (2016) RNA G-quadruplexes and their potential regulatory roles in translation. *Translation* **4**, e1244031
89. Murat, P., Guilbaud, G., and Sale, J. E. (2020) DNA polymerase stalling at structured DNA constrains the expansion of short tandem repeats. *Genome Biol.* **21**, 209
90. Lemmens, B., Van Schendel, R., and Tijsterman, M. (2015) Mutagenic consequences of a single G-quadruplex demonstrate mitotic inheritance of DNA replication fork barriers. *Nat. Commun.* **6**, 8909
91. Williams, S. L., Casas-Delucchi, C. S., Raguseo, F., Guneri, D., Li, Y., Minamino, M., *et al.* (2023) Replication-induced DNA secondary structures drive fork uncoupling and breakage. *EMBO J.* **42**, e114334
92. Groelly, F. J., Porru, M., Zimmer, J., Benainous, H., De Visser, Y., Kosova, A. A., *et al.* (2022) Anti-tumoural activity of the G-quadruplex ligand pyridostatin against BRCA1/2-deficient tumours. *EMBO Mol. Med.* **14**, e14501
93. Lipinski, C. A. (2000) Drug-like properties and the causes of poor solubility and poor permeability. *J. Pharmacol. Toxicol. Methods* **44**, 235–249
94. Saltzman, A. B., Leng, M., Bhatt, B., Singh, P., Chan, D. W., Dobrolecki, L., *et al.* (2018) gpGrouper: a peptide grouping algorithm for gene-Centric Inference and quantitation of bottom-up proteomics data. *Mol. Cell Proteomics* **17**, 2270–2283
95. Mergny, J.-L., Phan, A.-T., and Lacroix, L. (1998) Following G-quartet formation by UV-spectroscopy. *FEBS Lett.* **435**, 74–78
96. Serva, S., Weinhold, E., Roberts, R. J., and Klimasauskas, S. (1998) Chemical display of thymine residues flipped out by DNA methyltransferases. *Nucleic Acids Res.* **26**, 3473–3479
97. Monchaud, D., Allain, C., and Teulade-Fichou, M.-P. (2006) Development of a fluorescent intercalator displacement assay (G4-FID) for establishing quadruplex-DNA affinity and selectivity of putative ligands. *Bioorg. Med. Chem. Lett.* **16**, 4842–4845
98. Moorhouse, A. D., Santos, A. M., Gunaratnam, M., Moore, M., Neidle, S., and Moses, J. E. (2006) Stabilization of G-quadruplex DNA by highly selective ligands via click chemistry. *J. Am. Chem. Soc.* **128**, 15972–15973

99. Drewe, W. C., Nanjunda, R., Gunaratnam, M., Beltran, M., Parkinson, G. N., Reszka, A. P., *et al.* (2008) Rational design of substituted diarylureas: a scaffold for binding to G-quadruplex motifs. *J. Med. Chem.* **51**, 7751–7767
100. Kumari, S., Bugaut, A., Huppert, J. L., and Balasubramanian, S. (2007) An RNA G-quadruplex in the 5′ UTR of the NRAS proto-oncogene modulates translation. *Nat. Chem. Biol.* **3**, 218–221
101. Mergny, J.-L., and Maurizot, J.-C. (2001) Fluorescence resonance energy transfer as a probe for G-quartet formation by a telomeric repeat. *ChemBioChem* **2**, 124–132
102. Karsisiotis, A. I., Hessari, N. M., Novellino, E., Spada, G. P., Randazzo, A., and Webba da Silva, M. (2011) Topological characterization of nucleic acid G-quadruplexes by uv absorption and circular dichroism. *Angew. Chem. Int. Ed.* **50**, 10645–10648
103. Kypr, J., Kejnovská, I., Renciuk, D., and Vorlícková, M. (2009) Circular dichroism and conformational polymorphism of DNA. *Nucleic Acids Res.* **37**, 1713–1725
104. Smiatek, J., Chen, C., Liu, D., and Heuer, A. (2011) Stable conformations of a single stranded deprotonated DNA i-motif. *J. Phys. Chem. B* **115**, 13788–13795
105. Luo, Y., Granzhan, A., Marquevielle, J., Cucchiarini, A., Lacroix, L., Amrane, S., *et al.* (2023) Guidelines for G-quadruplexes: I. In vitro characterization. *Biochimie* **214**, 5–2313
106. Trantírek, L., Štefl, R., Vorlíčková, M., Koča, J., Sklenářář, V., and Kypr, J. (2000) An A-type double helix of DNA having B-type puckering of the deoxyribose rings. *J. Mol. Biol.* **297**, 907–922
107. Mizunuma, M., Suzuki, M., Kobayashi, T., Hara, Y., Kaneko, A., Furukawa, K., *et al.* (2023) Development of Mn2+-specific biosensor using g-quadruplex-based DNA. *Int. J. Mol. Sci.* **24**, 11556
108. Marzano, M., Falanga, A. P., Dardano, P., D'Errico, S., Rea, I., Terracciano, M., *et al.* (2020) π–π stacked DNA G-wire nanostructures formed by a short G-rich oligonucleotide containing a 3′–3′ inversion of polarity site. *Org. Chem. Front.* **7**, 2187–2195